

UNIVERSIDADE DE LISBOA
FACULDADE DE CIÊNCIAS
DEPARTAMENTO DE FÍSICA



Carbon ion radiography and tomography: a Monte Carlo study

Tiago Miguel dos Santos Marcelos

Dissertação da Tese de Mestrado
Mestrado Integrado em Engenharia Biomédica e Biofísica
Perfil em Radiações em Diagnóstico e Terapia

2014

UNIVERSIDADE DE LISBOA
FACULDADE DE CIÊNCIAS
DEPARTAMENTO DE FÍSICA



Carbon ion radiography and tomography: a Monte Carlo study

Tiago Miguel dos Santos Marcelos



Dissertação da Tese de Mestrado orientada pela Professora Doutora Katia Parodi da Ludwig Maximilians Universidade de Munique e pelo Professor Doutor Luís Peralta da Universidade de Lisboa

Abstract

Imaging techniques play an increasingly important role for treatment planning and *in-situ* monitoring in ion beam therapy. In this thesis, a Monte Carlo study was performed in order to support a prototype detector for carbon ion radiography and tomography.

The dedicated prototype detector, developed by GSI Darmstadt and the Heidelberg University Clinic on the basis of a stack of 61 ionizations chambers, was assembled and tested experimentally. Its applicability to carbon ion based transmission imaging was investigated and the first results showed the potential of carbon ion radiography as an attractive low dose imaging modality. Although the feasibility of carbon radiography was demonstrated and encouraging results were obtained, it is necessary to investigate some of the still open questions.

The ultimate goal of the Monte Carlo simulations in this work is to develop a reliable tool to investigate some details related to ion transmission imaging applications that are difficult or time consuming to explore experimentally. At the same time, we want to support and complement the experimental work.

Overall, the findings of this thesis support the large potential of carbon ion radiography and tomography. We achieved low dose radiographies, 0.05 mGy, and low dose tomographies, 17.47 mGy, while maintaining the image quality.

Keywords: Monte Carlo; ion therapy; transmission imaging; ion radiography; ion tomography

Sumário

A importância das técnicas de imagiologia em terapia com iões tem vindo a crescer, seja no planeamento ou durante a monitorização do tratamento. Nesta tese é apresentado um estudo Monte Carlo que suporta um protótipo de um detector para radiografia e tomografia com iões de carbono.

Este detector dedicado, desenvolvido pelo GSI Darmstadt e pela Universidade de Heidelberg, é constituído por 61 câmaras de ionização e foi construído e testado experimentalmente. A sua aplicação em imagiologia de transmissão com iões de carbono foi investigada e os primeiros resultados mostraram o seu potencial como uma técnica alternativa que oferece uma baixa dose depositada. Embora a viabilidade da radiografia com iões de carbono tenha sido demonstrada e resultados encorajadores tenham sido obtidos, existe ainda a necessidade de continuar a investigar e responder às questões que se mantêm abertas.

O objectivo final desta tese é o de desenvolver uma ferramenta fiável, baseada em Monte Carlo, que nos permita investigar alguns detalhes da imagiologia de transmissão com iões de carbono que são difíceis e/ou que demoram muito tempo para explorar experimentalmente. Ao mesmo tempo queremos que esta ferramenta suporte e complemente os trabalhos experimentais.

Em suma, os resultados desta tese demonstram o grande potencial da imagiologia com iões de carbono visto que conseguimos obter radiografias e tomografias depositando uma dose baixa, 0.05 mGy e 17.47 mGy, respectivamente, mas mantendo a qualidade das imagens.

Palavras-chave: Monte Carlo; terapia com iões; imagiologia de transmissão; radiografia com iões, tomografia com iões

Acknowledgments

I would like to express my most sincere gratitude and appreciation to Professor Dr. Katia Parodi and to Dr. Ilaria Rinaldi, from the Ludwig Maximilians University of Munich, for giving me the opportunity to work in their research group. I would also like to thank them for all the guidance, expertise and patience during the past year.

I am particularly thankful to Dr. George Dedes and to Dr. Guillaume Landry for the daily discussions and for helping me solve some of the problems that I faced during my project. Also, a special thank you to David Hansen from the Aarhus University in Denmark and Thomas Tessonier from the Heidelberg University for their insight.

I thank Professor Dr. Luís Peralta, my supervisor in Portugal, for all the advice and for introducing me to the particle therapy world.

I thank all the colleagues from the medical physics department for welcoming me and for the daily lunches and free time activities that we all enjoyed together. And also, for the valuable discussions!

I must also acknowledge the Reitoria da Universidade de Lisboa for the financial support, under the ERASMUS program, that made this internship possible.

Um obrigado muito especial aos meus pais, Manuel Marcelos e Maria Dulcília Marcelos, cujo amor, afeição e encorajamento tornaram este estágio uma realidade. Embora a grande distância e as saudades, o seu apoio manteve-se inabalável. Quero também agradecer às minhas irmãs, Cláudia Marcelos e Patrícia Marcelos, por terem ajudado os meus pais a criarem-me e a educar, por serem um exemplo para mim e por me terem incentivado a estudar e a ir mais longe. Espero que um dia eu também possa ser um exemplo a seguir pelos filhos delas. Agora que completo mais esta fase da minha vida, espero que este marco os encha a todos de orgulho!

Finalmente, quero agradecer à Inês Santos pelo amor e carinho.

Contents

Abstract	i
Sumário	iii
Acknowledgments	v
Contents	vii
List of Figures	ix
List of Tables	xiii
List of Acronyms	xv
1 Introduction	1
2 Background	3
2.1 Ion Beam Therapy	4
2.1.1 The Heidelberg Ion Therapy Center	5
2.2 Physical Aspects of Ion Radiation Treatment	6
2.3 Scanned ion beam delivery at HIT	10
2.4 The role of imaging techniques in radiotherapy	12
2.5 Carbon ion radiography and tomography	14
2.6 Purpose of this thesis	17
3 Materials and Methods	19
3.1 The FLUKA code	19
3.1.1 FLUKA models relevant for ion beam therapy	20
3.2 Developed tools	22
3.2.1 FLUKA user routines	23
3.2.2 MATLAB routines	25
3.2.3 Validation of the simulation	26
3.2.4 Validation of the materials	29
3.3 Validation of the radiography	31

CONTENTS

3.4	Digital phantom	36
3.5	Compute cluster	37
4	Results and discussion	39
4.1	Dose estimation	39
4.2	Simulated carbon ions radiography	42
4.3	Simulated carbon ion tomography	53
5	Conclusion and Outlook	59
	References	61
	Appendices	67
A	FLUKA <i>source.f</i> user routine	69
B	FLUKA <i>comscw.f</i> user routine	75
C	Submitting a job to the Compute cluster	77
D	Read binary output files from FLUKA	79

List of Figures

2.1	Comparison of depth-dose distribution of a ~ 150 MeV proton beam, a 270 MeV/u carbon ions beam and a 21 MeV photon beam. The Bragg Peak (BP) is visible both for carbon ions and protons (Fokas, Kraft, An, & Engenhart-Cabillic, 2009).	4
2.2	Comparison of dose color-wash display superimposed onto a grey-scale Computed Tomography (CT) of photon (left) and proton (right) treatment plans. The target is marked with a red line. The isodose areas are 1, 10, 25, 50 and 67 Gy ranging from dark blue to red where dark blue is 1 Gy and red is 67 Gy (Roelofs et al., 2012).	5
2.3	Schematic of the most important components of Heidelberg Ion Therapy Center (HIT). The ions are produced in the source, accelerated in a linear accelerator (LINAC) and then in the synchrotron. The ions extracted from the synchrotron are then guided to the different rooms with the High Energy Beam Transfer (HEBT) (Kleffner, Ondreka, & Weinrich, 2009).	6
2.4	Schematic representation of Coulomb interaction of a proton (blue) with an atomic electron (red) (Goiten, 2008).	7
2.5	Projected mean range in water of ions used in therapy (Ziegler, 2004).	9
2.6	Carbon and proton measured Bragg curves with the same mean range. The measurement was performed in water using two ionization chambers. The signal was normalized to the same peak height (Schardt et al., 2007).	10
2.7	Depth-dose profile in water for carbon ions of increasing initial energies (Mairani et al., 2008).	10
2.8	Schematic diagram of the basic elements of a scanning system (Goiten, 2008).	11
2.9	Hounsfield Unit (HU) to Water Equivalent Path Length (WEPL) calibration curve used for carbon ion treatment planning (Rietzel, Schardt, & Haberer, 2007).	13
2.10	Basic elements of a ionization chamber. A volume of gas is enclosed within the region in which the electric field is applied. Electrons drift faster than ions due to their lower mass (Knoll, 2000).	15
2.11	Sketch of the experimental set-up including the Ionization Chamber (IC) stack (Rinaldi et al., 2013).	16

LIST OF FIGURES

2.12	Comparison between the carbon ion radiography (left) converted to Water Equivalent Thickness (WET) of the anthropomorphic Alderson head phantom, and the Digitally Reconstructed Radiography (DRR) from a X-ray CT (right) also converted to WET using the same X-ray to ion range calibration curved as used for the treatment planning (Rinaldi, Brons, Jakel, Voss, & Parodi, 2014).	17
3.1	Pre-Equilibrium Approach to Nuclear Thermalization (PEANUT) - Hadron-nucleus interaction models used in FLUKA (www.fluka.org).	21
3.2	Sketch of the FLUKA models for nuclear interactions relevant for heavy ion beam therapy applications (www.fluka.org).	22
3.3	Beam scanning pattern for the radiographic images. Scanning starts in RP1 and ends in RP9.	24
3.4	Range differences in water between simulated and tabulated values from HIT (top) with correspondent percentage error (bottom).	27
3.5	Example of measured distribution and corresponding simulations (normalized to the data) for carbon ion (299.94 MeV/u) beam in water, sampled at a depth of ≈ 1.5 cm, in the entrance channel (left), and of ≈ 16.5 cm, shortly before the BP (right). The double Gaussian fits to the experimental and to the simulated data are also shown.	28
3.6	BP position in the detector as a function of energy. The line indicates the parametric fit of equation 3.6. $R^2 = 0.9992$ and $RMSE = 0.6991$	32
3.7	Dependence of the BP position on Polymethyl Methacrylate (PMMA) thickness. The line indicates a linear fit to the data. $R^2 = 0.9987$ and $RMSE = 0.3565$	33
3.8	Projection of a simulated radiography of a homogeneous PMMA cylinder with 16 cm of diameter. The simulated values were converted to PMMA equivalent thickness. The simulated values (black dots) were plotted together with the know physical dimensions of the phantom (red line).	36
3.9	Top view of the PMMA cylindrical phantom with the physical dimension (left) and the position of the different rods (right). All dimensions are in mm. . . .	37
4.1	Depth dose deposition of a ^{12}C ion beam with initial energy of 409.97 MeV/u. The phantom, shaded in green, is an homogeneous PMMA cylinder with a diameter of 16 cm. The detector is shaded in yellow. The situation represents a central beam crossing the thickest part of the phantom.	40
4.2	Dose deposited in the phantom for different number of primaries (left) and for different lateral and vertical scanning step size (right). The simulation data (dots) was fitted (lines) with a linear fit (left) and with an inverse quadratic fit (right).	42
4.3	PMMA cylindrical phantom with inserts implemented in FLUKA. Transparency is added to show the inside of the phantom.	43
4.4	Comparison of radiographies of the cylindrical phantom with inserts.	44

LIST OF FIGURES

4.5	Comparison of the central section in the x direction from the radiographies shown in figure 4.4.	45
4.6	Simulated radiography for the same configuration with different number of primaries per Raster Point (RP).	46
4.7	NRMSE for different number of particles. The curve resulted from averaging 3 completely independent runs of the same radiography.	47
4.8	Comparison between lateral dose profiles when using different lateral stepping sizes. In red we have the lateral profile of a single beam spot and in black the resulting extended lateral profile. A zoom of the area of interest is shown and the mean and the standard deviation of that area is calculated.	49
4.9	Comparison between the true radiography of the cylindrical phantom with inserts and the simulation for 500 ions per RP. The lateral stepping used was 2 mm.	50
4.10	Cumulative distribution of the beam as obtained from the MC simulation. The x and y position of a single particle in the beam is randomly sampled according to this distribution. The beam shape can also be recognized. . . .	51
4.11	Comparison between the reconstructed radiographies with the new algorithm. The different lateral and vertical stepping used were 1 mm, 2 mm and 3 mm for the same low number of 100 ions per RP.	52
4.12	Comparison between a vertical section of the 1 mm and 2 mm stepping radiography in a non-interface region, $x = 0$ mm (right), and in an interface region, $x = -30$ mm (left). The true value is also shown. We also evaluate the use of <i>a priori</i> information in the reconstruction.	53
4.13	Top view of the PMMA cylindrical phantom showing the rotation direction for the tomography.	54
4.14	Comparison between the reconstruction (right) of the cylindric PMMA phantom with rods using a Simultaneous Algebraic Reconstruction Technique (SART) algorithm with 361 projections and the true one (left). A 2 mm lateral and vertical step size was used.	55
4.15	Central sections in the horizontal (left) and vertical direction (right) of the reconstructed CT and the true one.	56
4.16	Comparison between the same reconstruction with (left) and without (right) <i>a priori</i> beam shape information. These images result from a 361 projections SART reconstruction, 1 mm lateral stepping and 100 particles per RP. . . .	56
4.17	Central sections in the horizontal (left) and vertical direction (right) of the reconstructed CT with and without <i>a priori</i> information and the true one. .	57

List of Tables

3.1	Parameters of the double Gaussian fit to the lateral spreading of carbon ion beams with initial energy of 299.94 MeV/u in water. The data was sampled at a depth of ≈ 1.5 cm and ≈ 16.5 cm, in the entrance channel and shortly before the BP, respectively	29
3.2	Properties of the materials used in our simulations. The experimental values are the values tabulated and used in the Treatment Planning System (TPS) system at HIT	30
4.1	Average dose deposited in the phantom for different settings of the radiography	41
4.2	Dose deposited in the phantom and Normalized Root Mean Square Error (NRMSE) for the same radiography settings but different number of simulated primaries per RP	47

List of Acronyms

BAMS Beam Application Monitoring System

BC Bragg Curve

BME Boltzmann-Master-Equation

BP Bragg Peak

cCT ^{12}C Computed Tomography

CT Computed Tomography

DFG German Research Foundation

DNA Deoxyribonucleic Acid

DRR Digitally Reconstructed Radiography

FWHM Full Width Half Maximum

GINC Generalized IntraNuclear Cascade

HICT Heavy Ion CT

HIMAC Heavy Ion Medical Accelerator in Chiba

HIT Heidelberg Ion Therapy Center

HU Hounsfield Unit

IC Ionization Chamber

LMU Ludwig Maximilians University of Munich

MC Monte Carlo

MRI Magnetic Resonance Imaging

MWPC Multi-Wire Proportional Chamber

LIST OF ACRONYMS

NRMSE Normalized Root Mean Square Error

PEANUT Pre-Equilibrium Approach to NUclear Thermalization

PET Positron Emission Tomography

PMMA Polymethyl Methacrylate

RBE Radiobiological Effectiveness

RMSE Root Mean Square Error

RP Raster Point

RQMD Relativistic Quantum Molecular Dynamics Model

SART Simultaneous Algebraic Reconstruction Technique

TPS Treatment Planning System

WEPL Water Equivalent Path Length

WET Water Equivalent Thickness

WHO World Health Organization

Chapter 1

Introduction

The application of light ion beams (e.g., proton and carbon ions) to external beam radiotherapy is rapidly spreading worldwide and seems to be one of the most promising improvements to conventional treatments using photons and electrons (Schneider & Pedroni, 1995).

The main physical advantage of ion beam therapy is related to the characteristic depth-dose profile of ions in matter, the Bragg Curve (BC). The dose deposited by ions rises sharply near the end of their range, the so-called Bragg Peak (BP). The majority of the dose can be deposited at a particular range by controlling the initial beam energy, since the range of ions in matter is related to their energy (Goiten, 2008). But, there is still an open problem, range uncertainties. These uncertainties can be explained by the fact that we cannot use the data directly from a X-rays Computed Tomography (CT) to plan our treatment since photons and ions interact with matter in a completely different way, and by not having a full knowledge of the patient anatomy during treatment.

Imaging techniques play an increasingly important role for treatment planning and real time verification of the patient position and organ location during treatment (Testa et al., 2013). The aim of the project "A novel imaging technique for ion beam therapy: Ion Computed Tomography" is to develop a new prototype detector system for ion-based radiography and tomography applications that will help improve the overall quality of the ion beam treatments. Although the feasibility of ion radiography was already demonstrated and encouraging results were obtained (Schneider et al., 2004; Shinoda, Kanai, & Kohno, 2006; Rinaldi et al., 2014; Parodi, 2014), there is still much to improve. This project is sponsored by the German Research Foundation (DFG) and is being carried out by the Ludwig Maximilians

CHAPTER 1. INTRODUCTION

University of Munich (LMU), Heidelberg University Hospital and GSI Darmstadt.

In this thesis, Monte Carlo simulations have been performed in order to simulate the full process related to transmission based imaging techniques to investigate in detail some of the still open questions.

My 11 months internship took place at the medical physics department of LMU, which belongs to one of the largest physics faculty in Germany and is highly ranked in Europe, notable for being the best-ranked German university in this field according to the 2010 Times Higher Education World University Rankings (Education, 2013). My stay in Munich was supported by the ERASMUS program.

This thesis reflects my work during the internship and is organized in the following way. In chapter 2, I describe the physics of ion interactions with matter, how ions deposit dose in tissues and how pencil beam scanning is performed. I also discuss the role of transmission imaging techniques in ion beam therapy and explain some technical details. In chapter 3 the methods and the materials used in this work are explained and the simulations are validated. Chapter 4 includes all the relevant results obtained as well as a discussion. Finally, chapter 5 presents the conclusions and an outlook to the future of the project.

Chapter 2

Background

Cancer is a broad group of diseases involving unregulated cell growth. If the tumor is malignant, tumor cells intrude upon and destroy adjacent tissues. The tumor cells can also spread to other locations of the body using the blood stream or the lymphatic system, a process known as Metastasis (Seeley, Stephens, & Tate, 2007). According to the World Health Organization (WHO) cancer is the second most frequent cause of death in developed countries. The number of new patients will increase by 50% by 2020 and cancer will become the leading cause of death (WHO, 2008).

To treat cancer, 50% of all patients receive curative or palliative chemotherapy and/or radiation treatments. Most of the time, radiation therapy is performed with photons or electron beams because the related technologies are more available worldwide.

The goal of all radiotherapy modalities is to deliver as effective as possible dose to the tumor while sparing the surrounding healthy tissues or organs at risk. Radiation can lead to the death of the tumor cells by breaking the Deoxyribonucleic Acid (DNA) by means of a direct hit or by radiation-induced free radicals.

The physics of conventional radiation (e.g. photons and electrons) poses intrinsic limitations to the effectiveness of the treatment while ions (e.g. proton or carbon) exhibit a more selective energy deposit in depth, the Bragg Peak (BP) in figure 2.1, and a more favorable Radiobiological Effectiveness (RBE) (Krämer & Scholz, 2000).

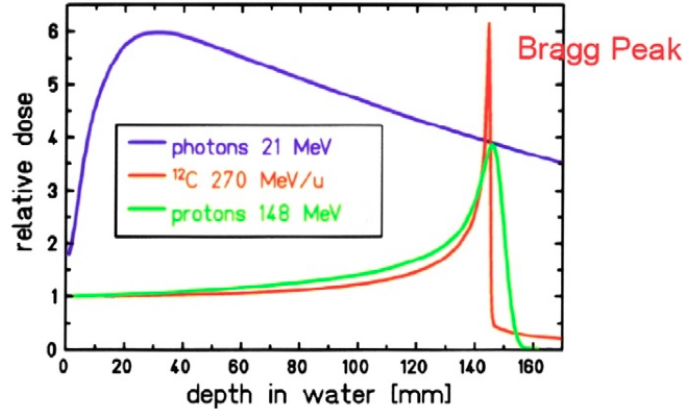


Figure 2.1: Comparison of depth-dose distribution of a ~ 150 MeV proton beam, a 270 MeV/u carbon ions beam and a 21 MeV photon beam. The BP is visible both for carbon ions and protons (Fokas et al., 2009).

2.1 Ion Beam Therapy

In 1946, Wilson proposed the use of charged hadrons in cancer therapy when he investigated the depth-dose profile of protons in a medium (Wilson, 1946). The first patients with deep located tumors were treated with protons in 1954 at the Lawrence Berkeley Laboratory in California, USA (Lawrence et al., 1958).

As Wilson mentioned, the main advantage of ion beam therapy is the superior physical selectivity of ions compared to photons or electrons, i.e. the inverse depth-dose profile as seen in figure 2.1. The dose deposited by ions is low in the entrance region and then increases sharply towards the end of the particle range with a rapid fall-off right after, resulting in a sharp and narrow peak, the so called Bragg Peak (BP) (Bragg & Kleeman, 1905).

The depth of the BP can be adjusted by selecting the proper initial energy of the ion beam which leads to a high conformal dose deposition in the tumor. Figure 2.2 compares the same radiation treatment using photons and protons and, as we can see, protons deposit much less dose to the healthy tissues surrounding the tumor than photons and, at the same time, offer a better tumor conformation (Roelofs et al., 2012).

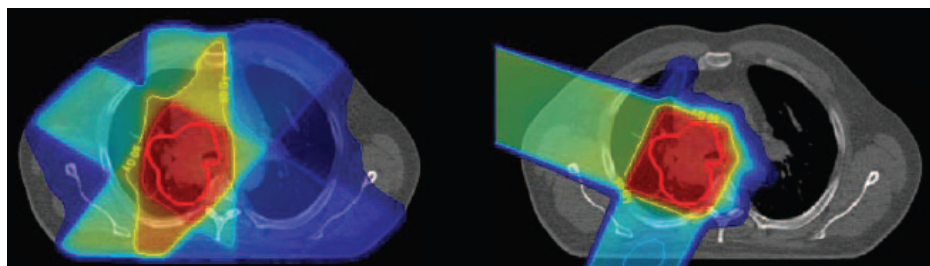


Figure 2.2: Comparison of dose color-wash display superimposed onto a grey-scale CT of photon (left) and proton (right) treatment plans. The target is marked with a red line. The isodose areas are 1, 10, 25, 50 and 67 Gy ranging from dark blue to red where dark blue is 1 Gy and red is 67 Gy (Roelofs et al., 2012).

2.1.1 The Heidelberg Ion Therapy Center

At the moment, 48 ion therapy centers are operative worldwide. According to the Particle Therapy Co-Operative Group (www.ptcog.ch), by December 2013, 106523 patients were treated in these centers using ion radiotherapy: 93746 with protons and 12777 with carbon ions.

The center relevant for my project is the Heidelberg Ion Therapy Center (HIT) in Germany which entered in operation in 2009 as the first dual proton and carbon synchrotron-based facility with an active beam delivery system. At HIT, there are two treatment rooms supplied with an horizontal beam, one treatment room with the first worldwide heavy ion gantry and a research room with an horizontal beam. A schematic of the HIT facility is shown in figure 2.3 (Kleffner et al., 2009).

Up to December 2013, 1871 patients were treated in Heidelberg, 1368 with carbon ions and 503 with protons. Irradiation with helium (^4He) and with oxygen (^{16}O) ions is also planned for the near future.

The flexible design of the HIT facility offers the possibility to investigate which ion species is the superior one for the treatment of certain tumors. An open debate regards the cost-benefit of ion beam therapy, since the construction of a combined ion beam therapy facility is really expensive. HIT had a total construction cost of 119 million Euro. The treatment cost per patient is about 20000 Euro, which is double or triple the cost of a conventional radiation treatment. But this new therapeutic modality can benefit even patients for whom no effective treatment has been available in the past.

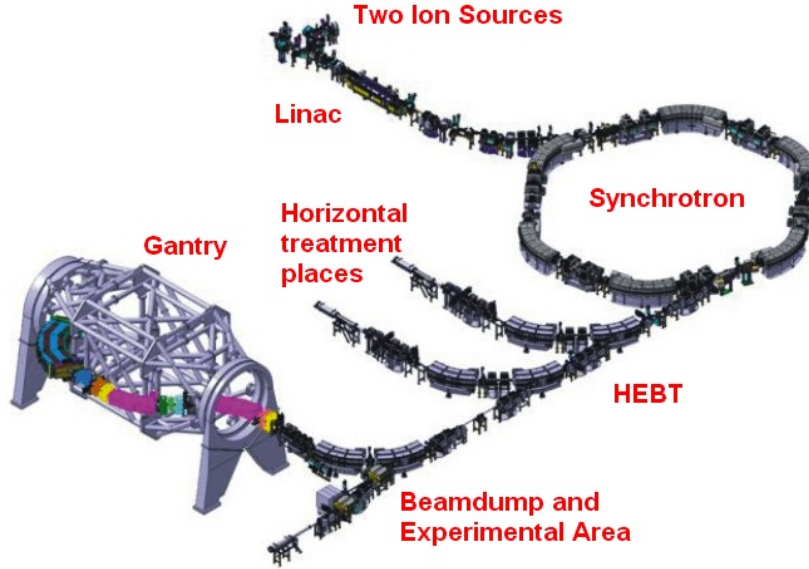


Figure 2.3: Schematic of the most important components of HIT. The ions are produced in the source, accelerated in a linear accelerator (LINAC) and then in the synchrotron. The ions extracted from the synchrotron are then guided to the different rooms with the High Energy Beam Transfer (HEBT) (Kleffner et al., 2009).

2.2 Physical Aspects of Ion Radiation Treatment

Protons and carbon ions lose energy while traveling through matter in a manner that is distinctly different from uncharged radiation (X-rays, γ -rays and neutrons). Ions lose kinetic energy gradually in matter leading to a finite range inside a medium (Goiten, 2008).

When ions of a given energy pass through matter they are subject to three main phenomena: Coulomb interactions with atomic electrons, Coulomb interactions with atomic nuclei and nuclear interactions with atomic nuclei. There are other processes through which the ions can lose energy such as emission of Cherenkov radiation and Bremsstrahlung. However, in comparison to the three main phenomena here stated, the energy loss is extremely low and for this reason they can be neglected (Goiten, 2008; Turner, 2007).

In ion radiation treatments, beam particles usually have a kinetic energy ranging from 70 to 500 MeV/u. In this range, particles transfer most of their energy to the traversed medium in inelastic Coulomb collisions with orbiting electrons of atoms.

The opposite charges of atomic electrons and impinging ions cause the ions to attract the electrons. Some electrons can be ejected out of the atom resulting in the ionization of

CHAPTER 2. BACKGROUND

the atom. These ejected electrons can further ionize other atoms in the neighborhood. In figure 2.4 we have a schematic of this process with a proton (Goiten, 2008).

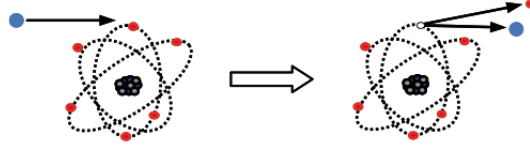


Figure 2.4: Schematic representation of Coulomb interaction of a proton (blue) with an atomic electron (red) (Goiten, 2008).

These interactions cause charged particles to lose energy by transferring it to atomic electrons. Due to the mass difference between these particles, only a small fraction of energy is transferred in each interaction. The Bethe-Bloch formula (Bethe, Rose, & Smith, 1938) describes how much energy a particle loses on average per unit path length. In equation 2.1 we have the electronic stopping power for energies above 1 MeV/u:

$$-\frac{dE}{dx} = 2\pi r_e^2 m_e c^2 N_e \frac{Z^2}{\beta^2} \left[\ln \left(\frac{2m_e c^2 W_{max} \beta^2 \gamma^2}{\langle I^2 \rangle} \right) - 2\beta^2 - 2\frac{C}{Z_t} - \delta \right] \quad (2.1)$$

where Z is the particle charge, β is the velocity of the particle scaled to the speed of light c , r_e and m_e are the electron classical radius and rest mass, respectively, W_{max} is the maximum energy transfer, N_e and I are the electron density and ionization potential of the medium of atomic number Z_t , C and δ are respectively the energy and absorber dependent shell and density corrections.

In figure 2.1 we have a depth-dose distribution of a proton and a carbon ion beams in water showing the characteristic BP. From equation 2.1 it is possible to understand the typical shape of the Bragg curve: as ions slow down the energy loss rate increases, i.e. their kinetic energy decreases along the penetration depth resulting in an abrupt rise of energy loss at low residual energy values. This happens in the last few millimeters of the particle path. When the particles completely stop we have a sharp reduction of the stopping power. This abrupt maximum followed by a sharp reduction is known as the BP. The depth at which the BP occurs depends on the initial energy of the particle beam, the higher the energy the deeper the range (Bragg & Kleeman, 1905).

Since the stopping power also decreases before the complete stop of the particles, the Bethe-Bloch formula has to be extended to low energies by replacing the particle charge Z

CHAPTER 2. BACKGROUND

by an effective charge Z_{eff} , which depends on the particle speed (Barkas, 1963):

$$Z_{\text{eff}} = Z \left(1 - e^{\alpha\beta Z^{-\frac{2}{3}}} \right) \quad (2.2)$$

This is necessary because, at lower energies (i.e., for ion velocities comparable to the electron orbital velocity), we have to take into account the mean charge redistribution due to the dynamic loss and capture of electrons from the target.

In clinical applications it is important to know the absorbed dose in the patient and the average range of the incident ions. This absorbed dose is correlated to the spatial distribution of energy deposited in a medium by the primary ions or other secondary particles and can be described by the following equation:

$$D = \frac{\Phi}{\rho} \frac{dE}{dx} \quad (2.3)$$

where D is the macroscopic dose delivered by a fluence Φ of mono-energetic charged particle beam to a medium of density ρ . This equation assumes that the energy carried in and out of a volume by secondary electrons is on average the same, hence the direct link to the average loss dE/dx of the ions (Rinaldi, 2011).

The average range of the incident ions refers to the length of the finite mean path traveled by a particle in a medium. Since the stopping power dE/dx describes the loss rate at which charged particles continuously slow down, the mean range R can be calculated by the integral of the inverse of dE/dx

$$R = \int_{E_0}^0 \left(\frac{dE}{dx} \right)^{-1} dE \quad (2.4)$$

where E_0 is the initial energy of the particle. Figure 2.5 compares the projected mean range in water of different ions used in therapy.

We should notice that the Bethe-Bloch formula (equation 2.1) describes the mean stopping power of a single charged particle. In a bunch of particles traveling through a medium the number of collisions and the energy loss per interaction fluctuate. This fluctuation results in a broadening of the BP due to range and/or energy straggling. The range straggling depends on the mass of the projectile and it varies approximately as the inverse of the square root of the particle mass. This results in a narrower BP with a steeper distal fall-off for heavier ions (Schardt et al., 2007; Mairani et al., 2008). Figure 2.6 compares the Bragg curve

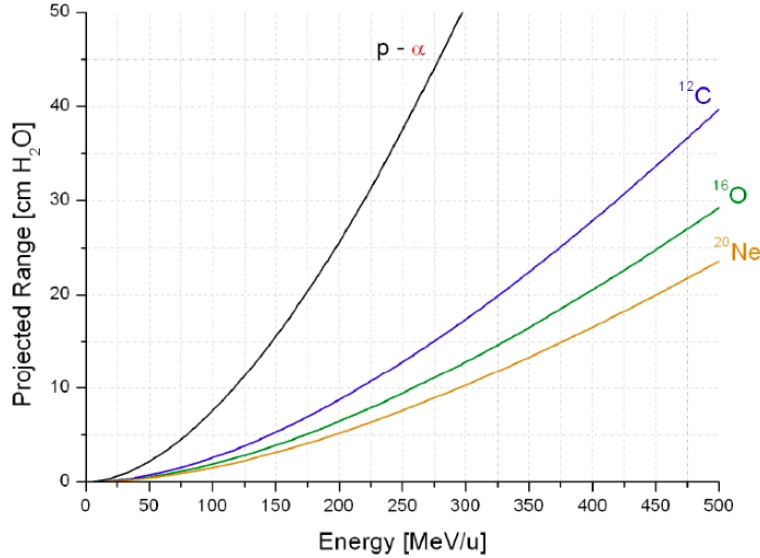


Figure 2.5: Projected mean range in water of ions used in therapy (Ziegler, 2004).

of a proton with a carbon ion beam where this effect is noticeable, and figure 2.7 shows the increase of the range straggling with the depth penetrated in a medium, resulting in broadened BPs with smaller height for higher initial energies.

The dose deposited in a medium is not only given by the depth profile but also by lateral spreading because charged particles, while transversing through a material, experience not only interactions with the target electrons but also multiple elastic collisions with target nuclei. These multiple interactions between ions and target nuclei give rise to a lateral spread of the beam. Beams of carbon and heavier ions show little scattering while proton beams show about three times more for equivalent conditions. This scattering of protons is similar or worse than that of photons at large penetration depths (Parodi, 2004).

Carbon ions penetrating a thick absorber experience strong nuclear force interactions that result in projectiles and/or target nuclei fragmentation (Golovkov, Aleksandrov, Chulkov, Kraus, & Schardt, 1997). Since charged fragments have about the same velocity as the primary ions but a lower charge Z , they have a larger range than that of the primary ions resulting in dose deposited even behind the BP, leading to the observed dose tail for heavy ($Z > 1$) ions, as seen in figure 2.7. Protons also experience nuclear interactions but fragments are not produced.

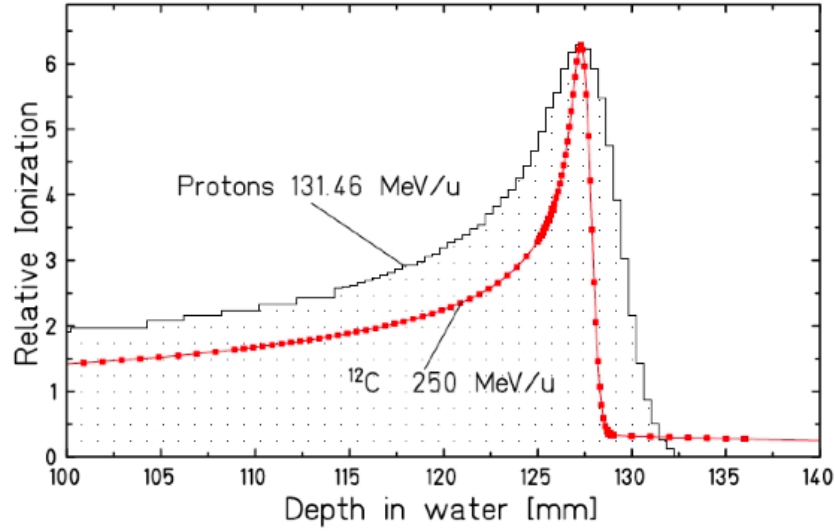


Figure 2.6: Carbon and proton measured Bragg curves with the same mean range. The measurement was performed in water using two ionization chambers. The signal was normalized to the same peak height (Schardt et al., 2007).

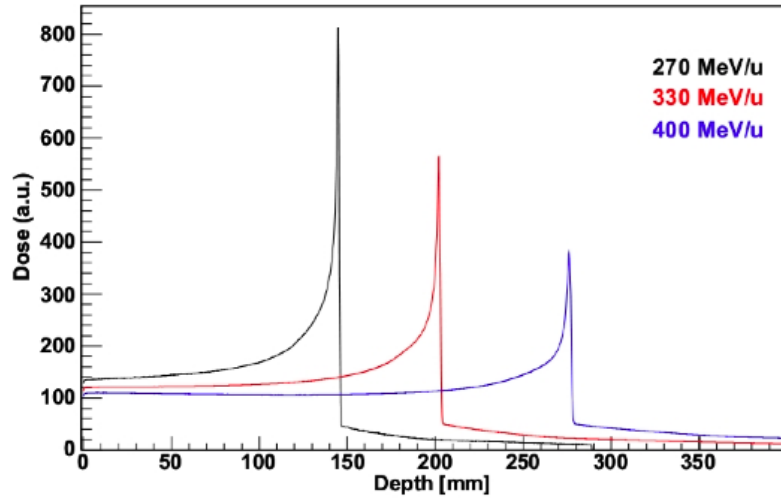


Figure 2.7: Depth-dose profile in water for carbon ions of increasing initial energies (Mairani et al., 2008).

2.3 Scanned ion beam delivery at HIT

Tumor size typically ranges from a few millimeters to several centimeters in diameter. In order to cover these volumes the beam extracted from an accelerator needs to be distributed

CHAPTER 2. BACKGROUND

laterally. There are two main beam delivery approaches for distributing the beam laterally, passive and active. We will focus on active beam scanning since it is what is installed at HIT (Haberer, Becher, Schardt, & Kraft, 1993).

The beam delivery system used at HIT plays a fundamental role for the imaging purposes investigated in this work. At HIT, a synchrotron is used to accelerate the particles to the necessary energy, i.e., to achieve the necessary depth in the patient. Then, these particles are extracted to the beam transport system that conducts the beam to one of the treatment rooms. A synchrotron demands a sequential process of particle injection, acceleration and extraction. When the extraction ends, the settings of the synchrotron are changed in preparation for the new injection. When the extracted beam leaves the vacuum pipe, it travels through a stack of independent Ionization Chambers (ICs) and Multi-Wire Proportional Chambers (MWPCs) within the Beam Application Monitoring System (BAMS). This detector system is used to control the beam position, beam dimension, fluence and for feedback to the raster scanning control system (Kleffner et al., 2009).

In active scanning systems, the beam is distributed laterally by variable strength magnets, which can rapidly vary the applied magnetic field. Scanning sweeps a narrow beam through the target volume in a predetermined pattern, depositing dose wherever it is needed. Each BP is delivered with the desired intensity.

Usually, the scan is implemented by a sequence of static narrow beams in which, after one beam has been delivered, the beam is moved to another position in the sequence. Figure 2.8 shows a schematic of the basic elements of the scanning system.

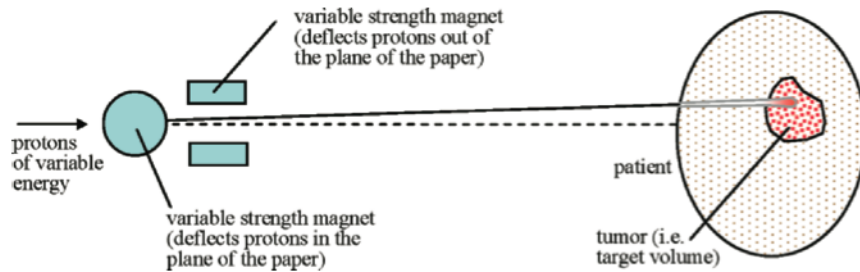


Figure 2.8: Schematic diagram of the basic elements of a scanning system (Goiten, 2008).

In the raster scan technique, an optimized 3D dose distribution is delivered to the tumor using different 2D fluence distributions, i.e., varying the number of stopping particles per

CHAPTER 2. BACKGROUND

squared millimeter from one lateral scan position to another, at fixed initial energy. This results in a division of the tumor volume in different isoenergy slices. By varying the beam energy in the accelerator, different depths can be achieved. Each slice is "painted" using two fast scanning magnets that deflect the beam in the transversal horizontal and vertical directions. The scanning magnets give us the x and y coordinates of the Raster Point (RP) regarding the isocenter, and the beam energy the depth of the slice (Rinaldi, 2011).

Scanned beam delivery systems have several advantages over passive beam delivery systems. Firstly, any shape of possible dose distribution can be achieved, by varying the strength of the magnets, making passive shaping systems unnecessary. Secondly, it uses particles very efficiently when compared with passive scattering in which only a fraction of the beam is uniform enough to be used for treatments. Thirdly, we can have narrow beams with different energies and weights. Since there is no need for patient-specific hardware, therapist do not need to enter and leave the room between irradiation fields to change this hardware. Finally, the neutron background is substantially reduced as a result of no interactions with a scattering material (Goiten, 2008).

2.4 The role of imaging techniques in radiotherapy

An ion beam treatment planning starts with an imaging technique, Magnetic Resonance Imaging (MRI), CT and/or Positron Emission Tomography (PET). The so called "planning CT", measures the photon attenuation coefficient μ in a specific tissue x . The μ_x is then converted to Hounsfield Unit (HU) scale using the attenuation coefficient in water μ_{H_2O} :

$$HU_x = 1000 \times \frac{\mu_x - \mu_{H_2O}}{\mu_{H_2O}} \quad (2.5)$$

where HU_x is a normalized value of the measured μ_x for a specific tissue. By definition, HU_{H_2O} is 0 and HU_{air} is -1000 . To obtain the range of the ion beam in Water Equivalent Thickness (WET) an experimentally validated calibration curve of the Water Equivalent Path Length (WEPL) is used (figure 2.9).

The WET is a way to state the range of a heavy charged particle beam after it penetrates a patient's body or other material in the beam line. The WEPL is a multiplication factor that, when multiplied by a thickness of a material, tell us what is the WET. In other words, the WET is obtained by integrating the WEPL of the media along the beam path. Further

CHAPTER 2. BACKGROUND

details about the WET and WEPL can be found in section 3.2.4.

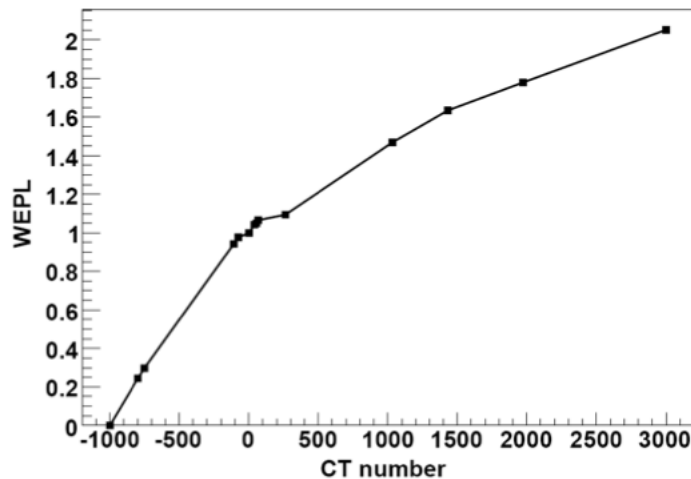


Figure 2.9: HU to WEPL calibration curve used for carbon ion treatment planning (Rietzel et al., 2007).

The error of the ion range calculated in patients is estimated to be between 1% and 3% due to non-unique correspondence between HU numbers and materials, experimental uncertainties in the CT image and in the calibration curve. This means that the range is uncertain in 1 to 3 mm in a depth of 10 cm. If the CT image would be replaced by a CT made with the ion used for the treatment, these errors could be reduced.

Besides these uncertainties, more errors can appear from artifacts (e.g. metallic implants in the patient), changes in the patient position or in the volume of some organs (e.g. lungs, bladder), accounting for approximate 5% to 20% deviations from the planned range (Jäkel & Reiss, 2007). These uncertainties can be reduced if tools for the visualization and monitoring of the particle distribution within the patient during irradiation are used (Jäkel & Reiss, 2007; Parodi, 2008).

Finally, there is some evidence that ion radiography and tomography deposit less dose in the patient than what is achieved today with x-rays (Schneider et al., 2004).

These are some of the reasons to develop an ion-based transmission imaging technique.

2.5 Carbon ion radiography and tomography

The first attempt to implement an Heavy Ion CT (HICT) was made in 2006 at the Heavy Ion Medical Accelerator in Chiba (HIMAC) in Japan. A broad carbon ion beam was used and the residual energy behind targets was measured (Shinoda et al., 2006; Ohno, Kohno, Matsufuji, & Kanai, 2004). The residual energy, measured by a calorimeter, has contributions from the primary ions as well as from fragmented ions. This dependence on the energy can make it difficult to discriminate, in the signal, the contributions from primaries or fragments. Fortunately, the BP position only depends of the primary ions which suggests the use of a range telescope instead of a calorimeter for HICT to measure the BP position (Rinaldi, 2011).

We will explain briefly how an ionization chamber operates since our prototype detector, a range telescope, is based on this type of radiation detector. Ionization Chambers (ICs) are the simplest of all gas-filled detectors. Their normal operation is based on collecting all charges created by direct ionization within the gas, by applying an electric field.

As a fast charged particle passes through a gas, molecules are excited and some others are ionized. After a neutral molecule is ionized, the resulting ion and free electron - ion pair - serve as the constituent of the electrical signal that the ionization chamber outputs. The practical quantity of interest is the total amount of ion pairs created inside the ionization chamber (Knoll, 2000).

In the presence of an electric field, the drift of the positive and negative charges, ions and electrons, create an electric current. The current in the external circuit is equal to the ionization current collected at the electrodes and with a sensitive ammeter placed in the external circuit we can measure the ionization current. Higher irradiation rate leads to higher current, if saturation effects are not present. In figure 2.10 we have the basic elements of an ionization chamber (Knoll, 2000).

As stated in section 2.2, the trajectory of high energy carbon ions can be assumed to be straight reducing the complexity of image reconstruction purposes. The disadvantage of this technique concerns the financial and technical effort needed to accelerate the carbon ions to high energies, ≈ 400 MeV/u, and to deliver the beam with a suitable isocentric system, an heavy ion gantry.

At HIT, carbon ions can be accelerated to energies up to 430 MeV/u (e.g. WET of ≈ 33 cm) and the first worldwide heavy ion gantry is available (Kleffner et al., 2009) which make

CHAPTER 2. BACKGROUND

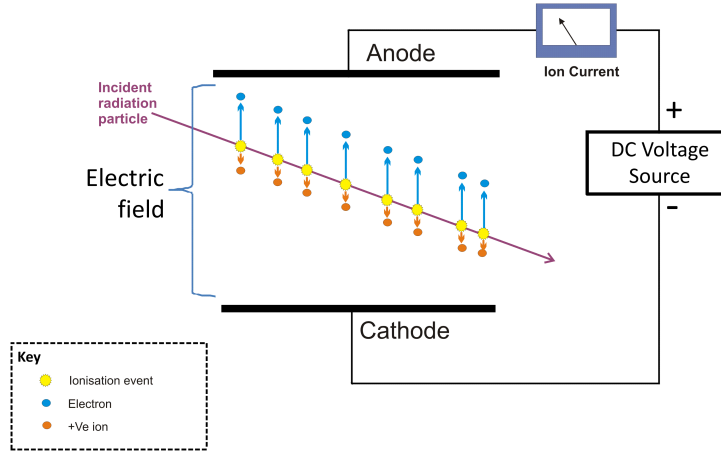


Figure 2.10: Basic elements of a ionization chamber. A volume of gas is enclosed within the region in which the electric field is applied. Electrons drift faster than ions due to their lower mass (Knoll, 2000).

it the perfect place to investigate HICT.

The first prototype detector from figure 2.11 results from the joint effort between GSI Darmstadt and the Heidelberg University Hospital. It consists of a stack of large-area parallel-plate ICs interleaved with absorber plates of homogeneous thickness serving as range degrader. The active cross section of each plate is $300 \times 300 \text{ mm}^2$ which is big enough for the scanning field of $200 \times 200 \text{ mm}^2$ available at HIT. The gas gap has a thickness of 6 mm and is filled with air because it is easier to operate and has almost the same performance as other gases, e.g. N_2 (Brusasco, 1999). The absorber plates consist of 3 mm slabs of Polymethyl Methacrylate (PMMA), since PMMA is made of elements with low atomic/mass number, similar to human tissue. The 3 mm slabs give the nominal resolution in depth of the IC stack and since the detector is constituted by 61 ICs, the maximum range covered by the detector is $\approx 21 \text{ cm}$ in WET (Rinaldi et al., 2013). The prototype detector is being upgraded and investigated in the context of the DFG project carried out by LMU, Heidelberg University Hospital and GSI Darmstadt.

In transmission imaging applications, the IC stack functions as a range telescope since we are only interested in locating the BP position estimated from the channel number with the maximum current.

The electronics, two I3200 32 channel digital electrometers from Pyramid Technical Consultants synchronized and buffered by an A500 module as real-time controller, were chosen

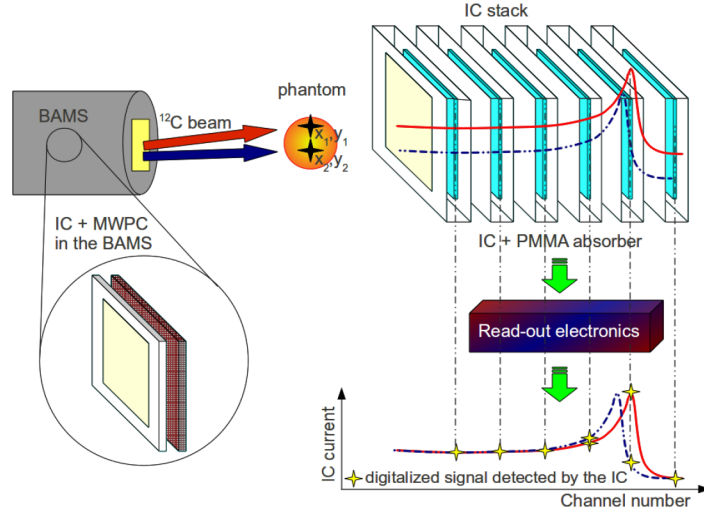


Figure 2.11: Sketch of the experimental set-up including the IC stack (Rinaldi et al., 2013).

because they are able to individually collect the integrated charge measured by all 61 ionization chambers. We should notice that the electrometer system measures 64 currents, from 1 pA to 50 μA (Rinaldi et al., 2013, 2014).

After the detector has been assembled, extensive characterization of the set-up in terms of beam parameters and settings of the read-out electronics was performed. This included a dependence of the IC stack measured signal with the number of beam particles per RP, an energy calibration that correlated the beam energy with the channel where the BP would be measured, and a dependence of the BP position when crossing different target thickness. The radiographic images were reconstructed and expressed in WET and a method to increase the range resolution of the IC stack was developed, as explained in (Rinaldi et al., 2013, 2014).

To perform a radiography of, e.g. an anthropomorphic Alderson head phantom (from Radiology Support Devices, Inc.), the phantom was positioned in the isocenter and irradiated with a laterally extended field, $250 \times 130 \text{ mm}^2$, of mono-energetic ^{12}C ions with an initial energy of 416.73 MeV/u and a beam spot of 3.4 mm Full Width Half Maximum (FWHM) delivered with a lateral and vertical raster scan stepping of 1 mm. The scan consisted of 32881 RPs and took $\approx 7 \text{ s}$ to be delivered (Rinaldi et al., 2014).

In figure 2.12 we have a comparison between a carbon ion radiography of the Anthropomorphic Alderson full head phantom and a traditional X-ray Digitally Reconstructed Radiography (DRR). This comparison showed a good correspondence, in terms of WET,

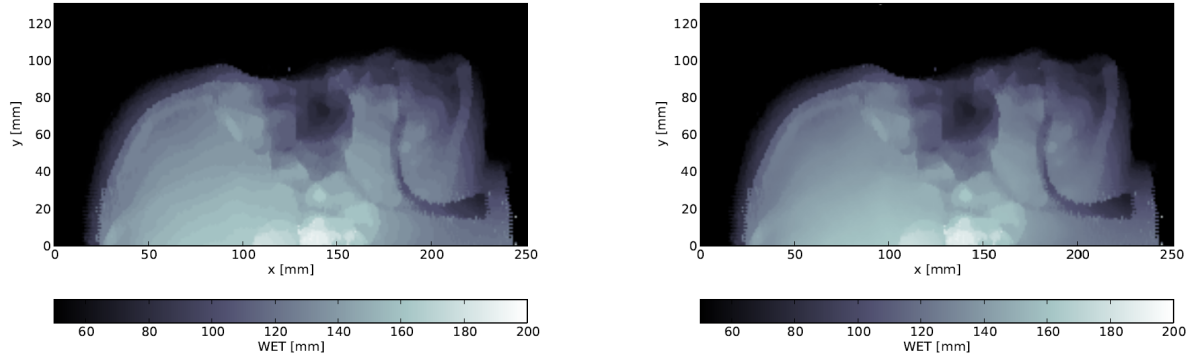


Figure 2.12: Comparison between the carbon ion radiography (left) converted to WET of the anthropomorphic Alderson head phantom, and the Digitally Reconstructed Radiography (DRR) from a X-ray CT (right) also converted to WET using the same X-ray to ion range calibration curved as used for the treatment planning (Rinaldi et al., 2014).

between the radiography obtained with carbon ions and the X-ray DRR. Further details and a more quantitative analysis can be found in (Rinaldi et al., 2014).

2.6 Purpose of this thesis

Although the feasibility of carbon ion radiography was demonstrated and encouraging results were obtained (section 2.5), there is still much to improve.

The purpose of this thesis is to develop a Monte Carlo based tool to investigate the performance of ion transmission imaging applications for configurations that are difficult or time consuming to explore experimentally. We would like to answer questions such as:

- What are the best settings for ion radiography using pencil beam scanning?
- What is the dose delivered to the patient per radiography?
- How can we reduce this dose without compromising the image quality?
- Is it possible to obtain a low dose ion tomography?
- Is ion tomography a real alternative to X-rays CT?

Besides answering some of these questions, the developed tool will allow us to support the developing of future versions of the prototype detector.

CHAPTER 2. BACKGROUND

In the following chapters the methods and the materials used in this thesis are explained, the relevant results are presented and discussed and finally, we draw some conclusions and give an outlook to the future of the project.

Chapter 3

Materials and Methods

3.1 The FLUKA code

Monte Carlo (MC) methods are a broad class of computational algorithms that rely on repeated random sampling to obtain numerical results. MC codes are useful tools in ion beam therapy to simulate the complex processes of ion interaction and propagation in matter.

FLUKA (FLUktuierende KAskade, www.fluka.org, (Battistoni et al., 2007; Ferrari, Sala, Fasso, & Ranft, 2011)) is a general purpose MC code for particle and heavy ion transport and interaction. It is developed and maintained in the framework of an agreement between the European Laboratory for Particle Physics (CERN) and the Italian National Institute for Nuclear Physics (INFN). FLUKA is capable of handling the transport and interaction of hadrons, heavy ions, and electromagnetic particles from 1 keV up to 20 TeV in any possible material and state.

At HIT, the FLUKA MC code was chosen as common computational platform. Several recent studies have reported comparisons between the FLUKA models and experimental data of interest for ion therapy, especially for carbon ion beams. These studies show that the agreement between FLUKA predictions and experimental data is very satisfactory, although there is still room for improvement (Sommerer et al., 2006; Parodi, Ferrari, Sommerer, & Paganetti, 2007; Mairani et al., 2010; Rinaldi et al., 2011; Parodi, Mairani, & Sommerer, 2013; Bauer et al., 2014).

FLUKA reads user input from an ASCII "standard input" file with extension `.inp`. The input consists of a variable number of "commands" (also called "options"), each consisting of

CHAPTER 3. MATERIALS AND METHODS

one of more "lines" (also called "cards" for historical reasons).

A user interface called FLAIR (FLUKA Advanced Interface) is also available and it offers features like easier creation of input files, debugging, compiling, running and monitoring the status of the simulation. It also includes a geometry editor. In this thesis we used FLUKA version 2011.2b.5 and FLAIR 1.2-4.

In order to support the user in the choice of the physics options to use, FLUKA offers default settings for specific problems. There are many different defaults but the one that was used in this thesis is the HADROTHE card which provides a default configuration for ion beam therapy applications. This card enables the use of predefined configurations and values for different options (e.g., production threshold of δ -rays, energy threshold for the transport of charged hadrons, neutrons, photons and electrons) that are best suited for ion beam therapy simulations. These defaults can also be changed if necessary.

For special problems the user can customize some FORTRAN routines called "user routines" to suit his/her needs. Two routines were extensively used within this thesis: the *source.f* and *comscw.f*. More details about the use of these routines can be found in section 3.2.1 and in appendix A and B.

3.1.1 FLUKA models relevant for ion beam therapy

In this section we will briefly explain the relevant FLUKA models for ion beam therapy. This information was adapted from the FLUKA manual and from the FLUKA courses available at www.fluka.org.

In FLUKA, the transport of charged particles is performed through an original Multiple Coulomb scattering algorithm (Ferrari, Sala, Guaraldi, & Padoani, 1992) supplemented by an optional single scattering method. The treatment of ionization energy loss is based on a statistical approach that provides a very good reproduction of average ionization and fluctuations (Fassò, Ferrari, Ranft, & Sala, 1997). Up-to-date effective charge parametrization is employed, and ion energy loss is described in "normal" first Born approximation with inclusion of charge exchange effects.

For the more complex nuclear processes, hadron-nucleus interactions up to 5 GeV and, therefore, relevant for ion therapy application (especially for protons), are handled by a Pre-Equilibrium Approach to NUClear Thermalization (PEANUT). PEANUT has been extensively validated against experimental data and can handle interactions of nucleons,

CHAPTER 3. MATERIALS AND METHODS

pions and kaons. The reaction mechanism (figure 3.1) is modeled in PEANUT by explicit Generalized IntraNuclear Cascade (GINC) smoothly joined to statistical pre-equilibrium emission (Gadioli & Hodgson, 1992; Griffin, 1967). At the end of the GINC and exciton chain, the evaporation of nucleons and light fragments is performed, following the Weisskopf treatment (Weisskopf & Ewing, 1940). Competition of fission with evaporation is taken into account with a statistical approach. Since the statistical evaporation model becomes less sound in light nuclei, the Fermi Break-up model (Fermi, 1950) is used instead. The excitation energy still remaining after the evaporation is dissipated via emission of γ -rays (Ferrari, Ranft, Roesler, & Sala, 1996). More details about PEANUT can be found in (Ferrari & Sala, 1997).

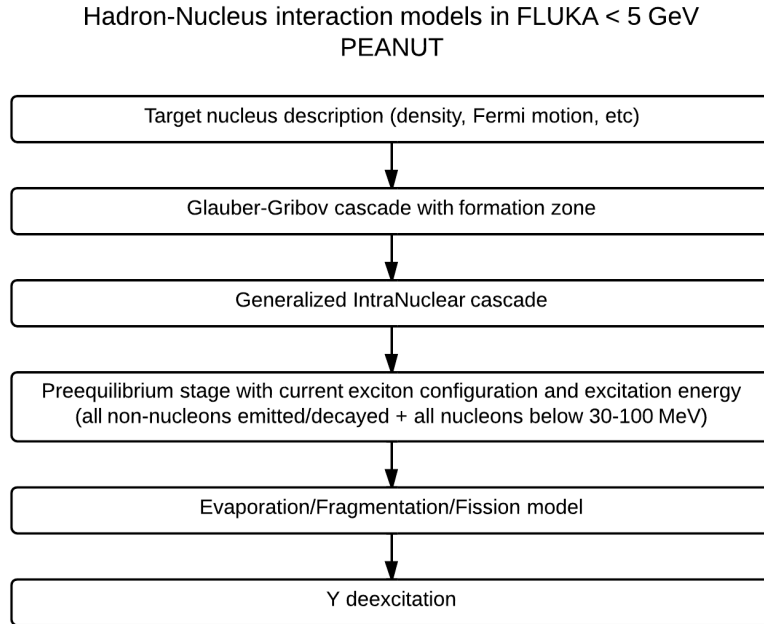


Figure 3.1: PEANUT - Hadron-nucleus interaction models used in FLUKA (www.fluka.org).

Nucleus-Nucleus interactions generated by heavy-ions ($Z > 1$) are treated through interfaces to external event generators. Two of them are relevant for ion beam therapy applications. For energies between 0.1 GeV and 5 GeV per nucleon an interface to a suitably modified Relativistic Quantum Molecular Dynamics Model (RQMD) is used. For energies below 0.1 GeV per nucleon down to the Coulomb barrier, a generator based on the Boltzmann-Master-Equation (BME) theory is used (Cerutti et al., 2006; Cavinato, Fabrici, Gadioli, Erba, &

Risi, 1998; Cavinato, Fabrici, Gadioli, Erba, & Riva, 2001). The excited pre-fragments resulting from these interactions can then undergo several additional steps, like evaporation, Fermi-Breakup, fission or γ -emission until they are completely de-excited and transported further by FLUKA. A sketch of the FLUKA models of nuclear interactions relevant for heavy ion beam therapy is given in figure 3.2. As we can see, for our simulations with carbon ions beam the models that are used by FLUKA are the BME and the RQMD.

Secondary radiation (e.g., neutrons, gammas, electrons) is also produced and transported by FLUKA.

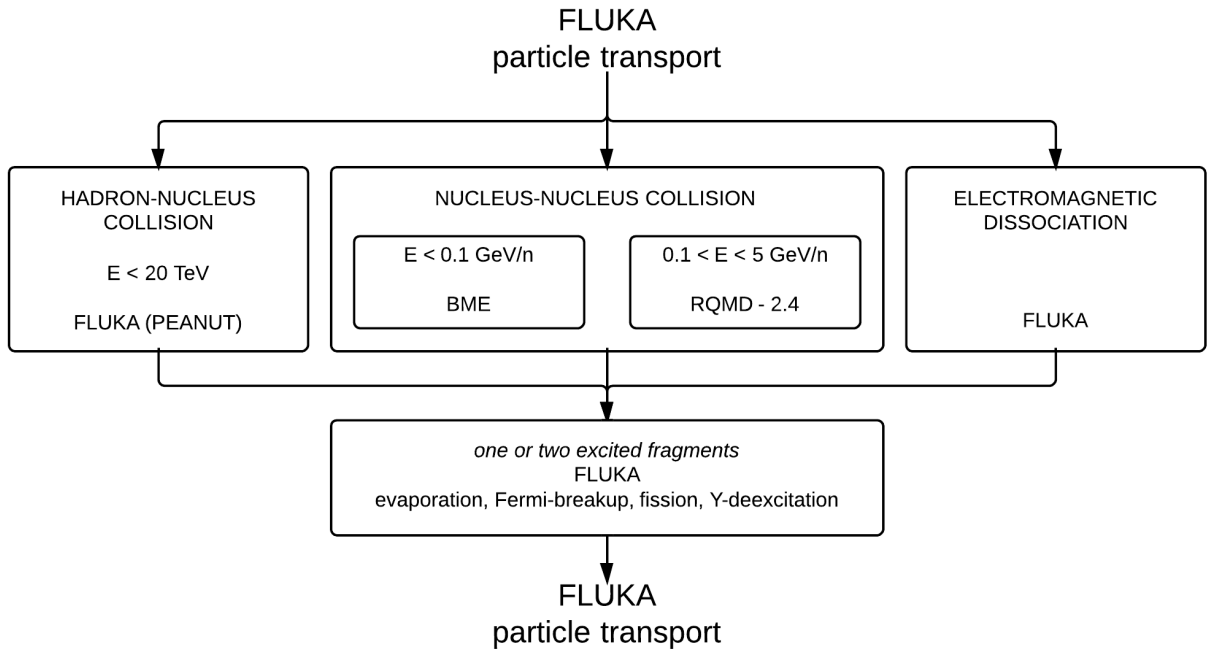


Figure 3.2: Sketch of the FLUKA models for nuclear interactions relevant for heavy ion beam therapy applications (www.fluka.org).

3.2 Developed tools

In this section the computation tools developed during the project will be explained.

3.2.1 FLUKA user routines

Due to the complexity of the problem at hands, special user routines had to be coded. Different user routines allow defining non-standard input and output, and, in some cases, even modifying to a limited extent the normal particle transport. Most of them are already present in the FLUKA library as dummy or template routines, and require a special command in the standard input file to be activated. Users can modify these routines, and even insert into them further calls to their own private ones. The routines used in this project were the *source.f* and *comscw.f*.

The user routine *source.f* is used to sample primary particle properties from distributions (e.g., in space, energy, time, direction, polarization or mixture of particles) too complicated to be described with the standard BEAM, BEAMPOS and POLARIZAti input cards. The specific values of the distributions can be read from a file, generated by some sampling algorithm, or just assigned.

With the user routine *comscw.f* it is possible to implement any desired logic to differentiate the returned scoring value according to information contained in the argument list (e.g., particle type, position, region, amount of deposited energy, particle generation).

The beam delivery system used at HIT plays a fundamental role for the imaging purposes investigated in this work. In order to produce simulated data as close as possible to the experimental data the beam line had to be described in the simulations. Since one of the parts of the beam line, the BAMS, is property of SIEMENS and is highly confidential, phase space files were used to describe the beam line.

A phase space is a space in which all possible states of a system are represented, with each possible state of the system corresponding to an unique point in the phase space. These phase space files include the kinetic energy, the x and y position and the cosine director of 20 million particles and they were generated for the 255 different energies available at HIT in a central beam spot 112.6 cm before the isocenter (phase space plane), i.e., right after the BAMS. Using the phase space files, the beam properties are well described and the properties and components of the BAMS remain protected since the user of the phase space files has no access to the description of the BAMS.

Since the HIT beam is delivered by an active scanning system, we had to include this feature in the simulation. The scanning pattern used for simulating radiographic images is shown in figure 3.3. The code let us control the field size, ranging from 0 to 20 cm in x and

CHAPTER 3. MATERIALS AND METHODS

y direction, and the vertical (step in y) and horizontal (step in x) distance between different RPs. For example, in order to get the 9 RPs showed in figure 3.3, we could scan a 2 by 2 cm² field with vertical and horizontal step of 1 cm. The scanning would start in raster point 1 (RP1), $(-1, 1)$, and end in RP9, $(1, -1)$, because the scanning system coordinates are always given with respect to the isocenter, $(0, 0)$, in this case RP5 (for a fixed $z = 0$).

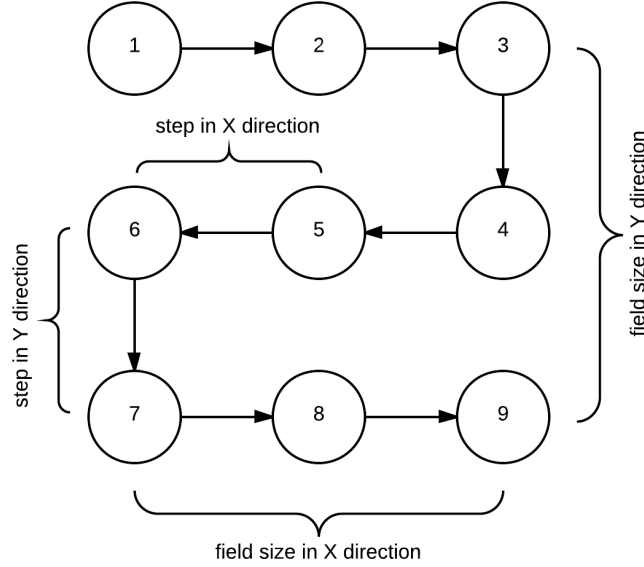


Figure 3.3: Beam scanning pattern for the radiographic images. Scanning starts in RP1 and ends in RP9.

At HIT, the scanning magnets of the horizontal and experimental rooms are positioned 650.6 cm before the isocenter $(0, 0, 0)$ (Bauer et al., 2014). Here, the magnets bend the beam in the x and y direction in order to irradiate different raster points at the isocenter. These bending angles have to be applied to every particle sampled from the phase space file, taking into account the values from the initial distribution originated by the undeflected central beam (i.e, cosine director and position of the particularly sampled particle).

In order to perform this operation, the cosine director vector from the space file has to be rotated around an arbitrary axis given by the cross product of the vector that joins the magnets position, the point at the isocenter we wish to irradiate (\mathbf{AB}) and, the forward direction vector. The necessary angle of rotation around the arbitrary axis is given by the dot product of those two same vectors. The rotation itself was computed using the Rodrigues' rotation formula. If \mathbf{v} is a vector in \mathbb{R}^3 and \mathbf{k} is a unit vector describing an axis of rotation

CHAPTER 3. MATERIALS AND METHODS

about which we want to rotate \mathbf{v} by an angle θ according to the right hand rule, we have:

$$\mathbf{v}_{\text{rot}} = \mathbf{v} \cos(\theta) + (\mathbf{k} \times \mathbf{v}) \sin(\theta) + \mathbf{k}(\mathbf{k} \cdot \mathbf{v})(1 - \cos(\theta)) \quad (3.1)$$

The derivation of the Rodrigues's rotation formula is shown in (Murray, Li, & Sastry, 1994). \mathbf{v}_{rot} is then passed to FLUKA as the new cosine director of the particle that was sampled.

Finally, we need to give FLUKA the coordinates of the particle where we want the transport to start. The new coordinates result from the sum of the sampled values from the phase space for x and y with the point of intersection of the vector \mathbf{AB} with the phase space plane.

All these operations (i.e, sampling from the phase space file, the rotation of the cosine director and the coordinate change according to the scanning pattern) are coded in the *source.f* user routine.

Moreover, we needed to score the energy deposited in the detector per raster point in order to be able to reconstruct the radiography. To get this information another user routine was used, the *comscw.f*. With this routine, the energy deposited inside our detector was recorded and passed to the *source.f* routine where, every time we changed raster point, the routine wrote the energy deposited in every channel of the detector to a binary file. Then, all values were reset and the process was repeated for another RP.

In the end of a full simulation run we get as output a binary file with a number of blocks equal to the number of RPs in the irradiated field. Each block has the energy deposited in every channel of the detector and the average dose given to the entire phantom for that RP. This file also includes an header with information about the simulation: field size, stepping size and the number of particles per RP.

The code, in FORTRAN, for the user routine *source.f* can be found in appendix A and for the user routine *comscw.f* in appendix B.

3.2.2 MATLAB routines

MATLAB (The Mathworks Inc., USA) routines were developed to read the binary output files from FLUKA (appendix D). Also, all data analysis was done by self-written routines in MATLAB.

3.2.3 Validation of the simulation

The FLUKA physics models were already extensively verified and validated as shown in (Sommerer et al., 2006; Parodi et al., 2007; Mairani et al., 2010; Rinaldi et al., 2011) and will not further be discussed in this thesis.

The ultimate goal of the simulations in this work is to develop a reliable tool to investigate the performance of ion transmission imaging applications for configurations that are difficult or time consuming to explore experimentally, and to complement the experimental work.

We started by simulating the range of a ^{12}C ions beam in water. For that, the beam was shot at a simple water phantom with entrance surface at the isocenter and then the BP position was found. A density of 0.9980 g/cm^3 was set to water, corresponding to a water temperature of 21°C . We also used an ionization potential for water of $I_w = 78\text{ eV}$ to agree with the measured Bragg curve at HIT. Each simulation was performed 5 times with 5000 primaries each in order to achieve good statistics. Different seeds were used for each cycle in order to have independent runs and a binning scoring of 0.1 mm was used. Then, this was repeated for 25 different relevant energies ranging from 277.19 to 430.10 MeV/u and we compared the simulation results with the tabulated values of HIT.

The differences of the beam range in water for different energies are shown in figure 3.4. The mean difference is 0.53 mm with a standard deviation of 0.11 mm . This overestimation of the range results in a percentage error that varies from 0.16% to 0.34% with the mean being 0.25% (figure 3.4), which proves a good agreement between the simulated data and the tabulated values.

The complex lateral spreading of ion beams in air and in the traversed tissue is typically approximated with ideal gaussian-shaped distribution since, when working with gaussian distributions, superimposition of several scattering contributions can be easily calculated (Schwaab, Brons, Fieres, & Parodi, 2011). At HIT, the Treatment Planning System (TPS) uses a double gaussian parametrization for scanned carbon ions beam in water as discussed in (Parodi et al., 2013).

An example of the validation of the implemented simulation framework against experimental values measured for line scans of carbon ions beams in water is shown in figure 3.5 in semi-logarithmic scale. The profiles were sampled in the plateau region and shortly before the BP for 3 different energies: 200.28 MeV/u , 299.94 MeV/u and 430.10 MeV/u . The experimental data resulted from the experimental campaign reported by (Schwaab et

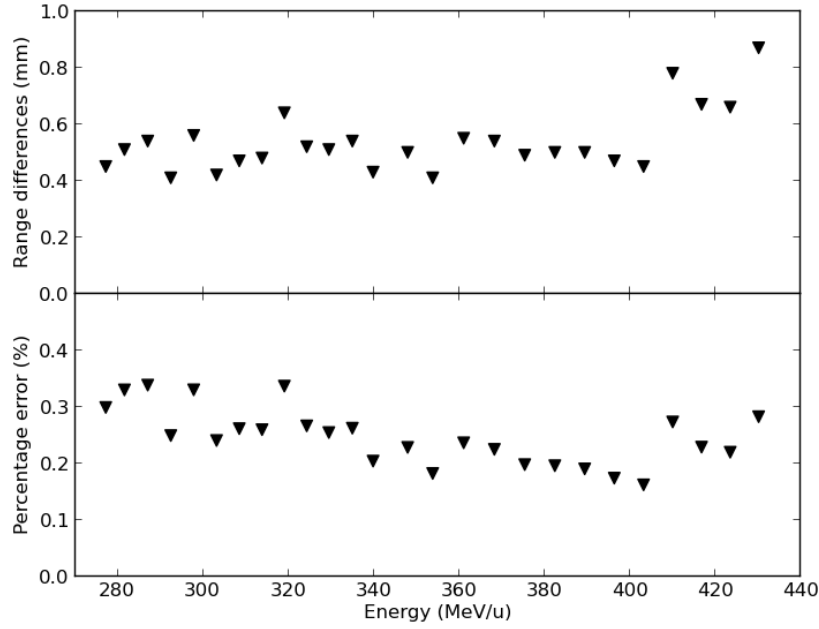


Figure 3.4: Range differences in water between simulated and tabulated values from HIT (top) with correspondent percentage error (bottom).

al., 2011) and the simulated data resulted from scanning an horizontal line of 10 cm with 1 mm stepping between each RP and scoring the deposited dose at different depths in a water phantom.

The simulated data was compared with the experimental data and a double gaussian distribution was fitted to both:

$$d(E, x, z_{eq}) = n \times [(1 - w) \cdot G_1(x, \sigma_1(z_{eq}, E)) + w \cdot G_2(x, \sigma_2(z_{eq}, E))] \quad (3.2)$$

where n is a normalization factor of the two gaussians of unitary area, w is their relative weight, x denotes the lateral distance to the beam center and z_{eq} is the depth in water.

If we assume that the spot is rotationally symmetric, i.e. the widths σ_1 and σ_2 are the same in x and y direction, we get a more general expression corresponding to our irradiation condition:

$$d(E, x, z_{eq}) = n \times \left[\frac{1 - w}{2\pi\sigma_1^2} \cdot \int dy e^{-\frac{x^2+y^2}{2\sigma_1^2}} + \frac{w}{2\pi\sigma_2^2} \cdot \int dy e^{-\frac{x^2+y^2}{2\sigma_2^2}} \right] \quad (3.3)$$

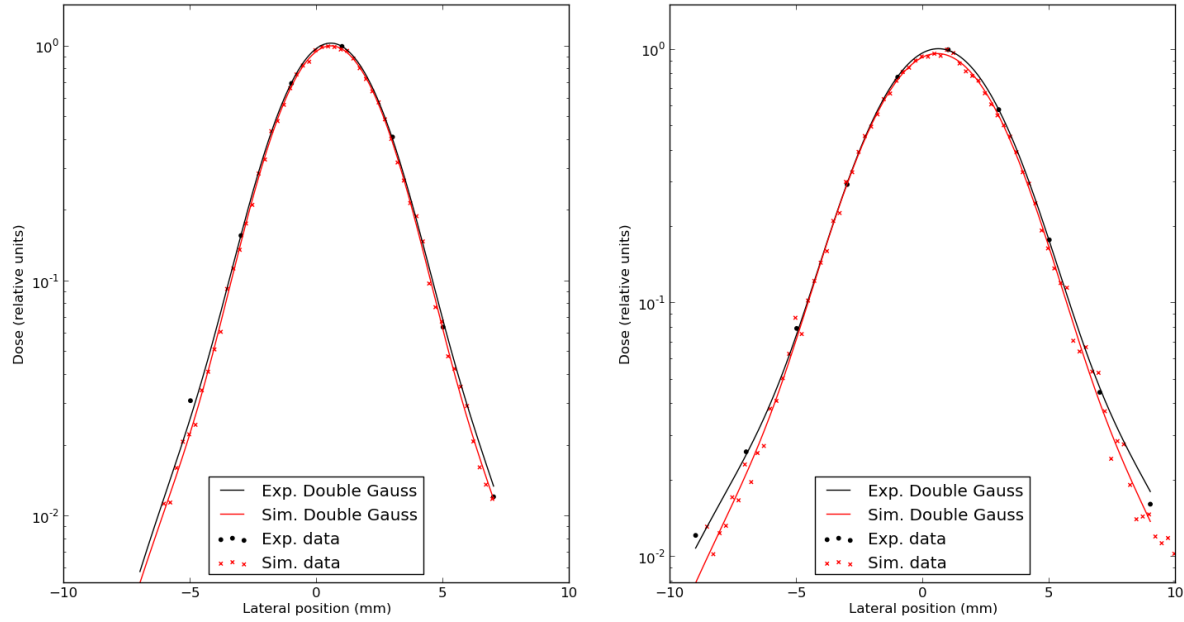


Figure 3.5: Example of measured distribution and corresponding simulations (normalized to the data) for carbon ion (299.94 MeV/u) beam in water, sampled at a depth of ≈ 1.5 cm, in the entrance channel (left), and of ≈ 16.5 cm, shortly before the BP (right). The double Gaussian fits to the experimental and to the simulated data are also shown.

where the parameters of interest from the fit are w and $(1 - w)$, the relative weights of the two normalized gaussians, σ_1 and σ_2 , their widths as a function of the beam initial energy and the water equivalent depths ($z_{eq} = 0$ for beam profiles in air). For the example shown in figure 3.5 we got the fitting parameters shown in table 3.1. We can see that the parameter that differs the most from the experimental and simulation fits is σ_2 but, in overall, the fitting parameters show a satisfactory agreement. The differences found can be partly explained by the fact that, at HIT, the lateral profile of the beam slightly changes from one day to the other due to different tunings of the synchrotron and extraction beam lines. The differences can also be partly explained by possible uncertainties in the nuclear models. For the other energies not shown here, the results were consistent with what has been shown in figure 3.5 and table 3.1.

It is also visible in figure 3.5 that the dose distribution of the beam gets broader with depth due to the scattering of the primary particle and to nuclear products emitted at large angles.

Parameters of the double Guassian fit

	$z_{eq} \approx 1.5$ cm		$z_{eq} \approx 16.5$ cm	
	Experimental	Simulation	Experimental	Simulation
σ_1 (mm)	1.7548	1.7336	2.1796	2.1970
σ_2 (mm)	4.2298	3.7278	4.7406	4.4102
w	0.0984	0.1005	0.1650	0.1577
$(1 - w)$	0.9016	0.8995	0.8350	0.8423

Table 3.1: Parameters of the double Gaussian fit to the lateral spreading of carbon ion beams with initial energy of 299.94 MeV/u in water. The data was sampled at a depth of ≈ 1.5 cm and ≈ 16.5 cm, in the entrance channel and shortly before the BP, respectively

3.2.4 Validation of the materials

In this section we test the properties of the materials used in the simulations performed throughout the work. The purpose is to verify the match between the WEPL of the materials used in the FLUKA simulations and the experimental values, and if necessary, we correct them. The WEPL is a multiplication factor that, when multiplied by a thickness of a material, tell us what is the WET. In other words, the WET is obtained by integrating the WEPL of the media along the beam path. The WET is a way to state the range of a heavy charged particle beam after it penetrates a patient's body or other material in the beam line:

$$\text{WET} = \Delta x \cdot \text{WEPL}_{\text{mat}} \quad (3.4)$$

For example, if a beam crosses 10 cm of PMMA, using equation 3.4 and knowing that the WEPL of PMMA is 1.165, we conclude that this PMMA thickness is equivalent to the beam having crossed 11.65 cm of water.

The protocol used in this thesis and at HIT to find the WEPL values is the one suggested by (Rietzel et al., 2007; Kurz, Mairani, & Parodi, 2012). We start by measuring the BP depth in water with no material in the beam line (BP), then we repeat the measurement with a known thickness of the material we are calibrating (Δd) and record this new BP position (BP_{mat}). If the simulation was performed in vacuum, as it was in our case, the WEPL of

CHAPTER 3. MATERIALS AND METHODS

the material is simply given by:

$$\text{WEPL}_{\text{mat}} = \frac{\text{BP} - \text{BP}_{\text{mat}}}{\Delta d} \quad (3.5)$$

if the simulation/measurement is performed in air we also have to take the air depth into account.

In table 3.2 we have the properties of the different materials we used in this thesis. PMMA is a default material in FLUKA and there was no need for an adjustment in its properties since the experimental WEPL value matched with the default value. On the other hand, the Lung and Cortical Bone tissue had to be introduced and adjusted. Since our objective is to match the simulated WEPL with the experimental value, we can change, for example, the density of the material in FLUKA to increase or decrease the WEPL. The constituents of these materials, i.e., percentage in weight of each element, are the same that we find in the tissue equivalent phantom rods from GAMMEX used at HIT. The introduced materials are specifically: LN-450-Lung for the lung tissue and SB3-Cortical-Bone for the Cortical bone.

Materials used in this work and their properties

	Experimental		FLUKA	
	ρ (g/cm ³)	WEPL	ρ (g/cm ³)	WEPL
PMMA	1.190	1.165	1.190	1.165
Lung	0.460	0.455	0.515	0.455
Cortical bone	1.823	1.618	1.910	1.615
Air	0.001	0.001	0.001	0.001

Table 3.2: Properties of the materials used in our simulations. The experimental values are the values tabulated and used in the TPS system at HIT

As we can see from table 3.2, the density of the lung and cortical bone had to be increased so that the WEPL would agree with the experimental values. If the material is a compound, FLUKA computes the ionization potential of the material by applying Bragg's rule of additivity to stopping power. In other words, the mass stopping power is obtained by a linear combination of the constituent stopping powers (ICRU Report 49, 1993; Paul, Geithner, & Jäkel, 2007) which, for more complex materials such as Lung or Bone, can lead

to less accurate results. For this reason, we decided to increase the density of these two materials instead of trying to find what would be the correct value for the ionization potentials. We should also notice that, from therapy center to therapy center, the value that is used for the ionization potential of water in Monte Carlo codes changes.

3.3 Validation of the radiography

The next step was to perform an energy calibration of the detector similar to what is explained in (Rinaldi et al., 2013, 2014) for the experimental setup.

The position of the BP inside the detector defines where most of the initial energy of the beam is deposited. Without any object in between, the position of the BP in the detector depends only on the initial energy of the particle beam. For higher energies the peak will appear deeper inside the detector while lower energies will result in a BP in the first channels of the detector.

For the energy calibration a simple PMMA phantom was used to model the range telescope. This phantom was 30 cm deep and divided in 100 channels of 3 mm thickness each, consistent with the dimensions of the PMMA absorber plates used in the IC stack. This simplified detector is bigger than the actual detector that has only 61 channels, i.e., 18.3 cm in depth in PMMA (21.3 cm in water). The reason behind this is simple: for higher energies the detector was not deep enough to stop the particles and for that reason, no BP was observed. Then, the calibration curve had to be extrapolated for those missing points. Using a bigger detector resulted in a more precise calibration curve.

Each simulation was performed 5 times with 5000 primaries each and different seeds for each cycle. In figure 3.6 we have the simulated energy calibration curve. The parametrization was done by fitting the data with the following expression:

$$BP_0(E) = a \cdot E^{1.75} + b \quad (3.6)$$

as a numerical fit to describe the dependence of the BP position BP_0 in function of the Energy (E) from a semi-empirical formula as presented in (Leo, 1987), where BP_0 is the channel number of the detector where the BP is located for the initial beam energy E . This

CHAPTER 3. MATERIALS AND METHODS

resulted in the following calibration curve:

$$\text{BP}_0(E) = 0.002177 \cdot E^{1.75} + 0.9174 \quad (3.7)$$

with a coefficient of determination $R^2 = 0.9992$ and a root mean square error $\text{RMSE} = 0.6991$. The parameter a has units of $(\text{MeV/u})^{-1.75}$ and b is dimensionless.

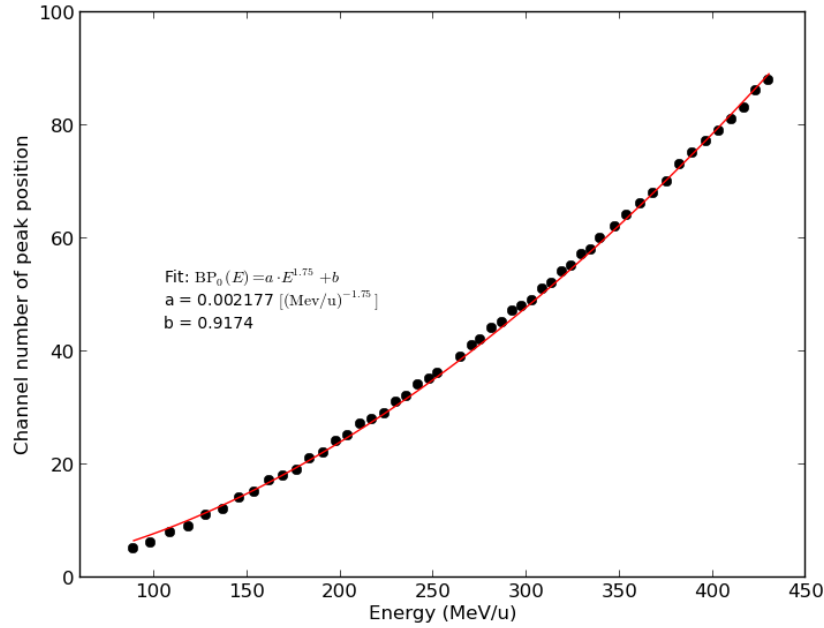


Figure 3.6: BP position in the detector as a function of energy. The line indicates the parametric fit of equation 3.6. $R^2 = 0.9992$ and $\text{RMSE} = 0.6991$.

Similarly to what was done for the beam energy calibration, a parametrization of the BP position as a function of target thickness was also performed. Using the same initial energy, 334.94 MeV/u, we used different PMMA thicknesses and checked in which channel of the detector the BP would be. The results are shown in figure 3.7. The step like structure of the data is due to the fact that each channel of detector has a finite nominal resolution of 3 mm of PMMA (3.495 mm of water). The parametrization was obtained as a linear fit to the data:

$$\text{BP}^{pos}(\Delta x_{\text{PMMA}}) = c \cdot \Delta x_{\text{PMMA}} + d \quad (3.8)$$

CHAPTER 3. MATERIALS AND METHODS

The linear dependence of the BP position, i.e., detector channel number, with the depth of PMMA transversed is clearly seen and can be expressed as:

$$\text{BP}^{pos}(\Delta x_{\text{PMMA}}) = -0.338 \cdot \Delta x_{\text{PMMA}} + 58.317 \quad (3.9)$$

with $R^2 = 0.9987$ and $\text{RMSE} = 0.3565$.

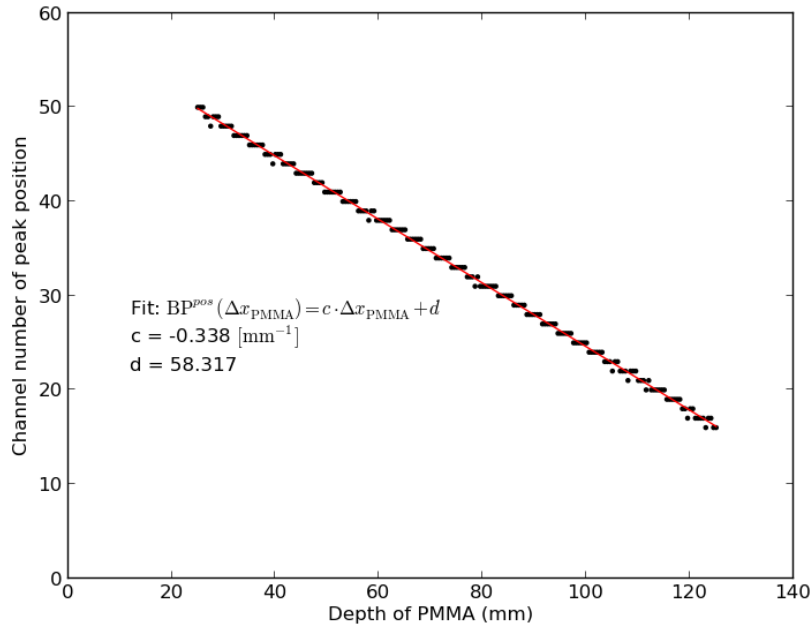


Figure 3.7: Dependence of the BP position on PMMA thickness. The line indicates a linear fit to the data. $R^2 = 0.9987$ and $\text{RMSE} = 0.3565$.

We should also notice that the parameter c , with units of mm^{-1} , is related to the thickness of each channel, i.e., $-1/c = 3.00 \text{ mm}$, which is the theoretical thickness of each PMMA slab in the detector. From the simulations we obtain $-1/c = 2.96 \text{ mm}$, which means that our c parameter has an error of $\approx 1.3\%$ when compared with the theoretical value. The parameter d gives us the channel number in the detector for a carbon ion beam with initial energy of 334.94 MeV/u , the energy used for this simulation, when there is no PMMA in the beam line, i.e., depth of 0 mm . Comparing our $d = 58.317$ with the value calculated with equation 3.6, $BP_0(334.94) = 58.006$, we see that the values agree quite well ($\approx 0.5\%$ error) showing once again the correctness of the simulation data. We should notice that the parameter d is energy dependent.

CHAPTER 3. MATERIALS AND METHODS

The parameters a , b , c and d have been experimentally determined in (Rinaldi et al., 2013) to be $a = 0.00219 \text{ MeV/u}^{-1.75}$, $b = 0.356$, $c = -0.306 \text{ mm}^{-1}$ and $d = 55.707$. The parameters c and d were determined using an initial beam energy of 334.94 MeV/u . Comparing these values with the ones from the simulations, since they were obtained with the same methods, we see that the parameter a agrees quite well with the experimental one but that is not the case for b , c and d . But, as shown in section 3.2.4, what really matters is the conversion to WET and, although the parameterizations are slightly different, in the end, the results agree quite well. The differences might be due to the simplified detector used in the simulations, where we approximated our detector as a homogeneous PMMA block which neglects the electrodes and the air gap, compared to the actual detector (see section 2.5). Also, some experimental errors and uncertainties might be present. For example, the PMMA in FLUKA is perfectly homogeneous but that might not be the case for the PMMA phantoms used in the experimental measurements. Additionally, the PMMA properties from the real detector slabs and the phantoms used might be different, while in FLUKA the PMMA is exactly the same.

By using both the energy parametrization (equation 3.7) and the thickness parametrization (equation 3.9), and knowing the WEPL value of PMMA (1.165), it is possible to express radiographic images in terms of WET using the following equation:

$$\text{WET} = -\text{WEPL}_{\text{PMMA}} \cdot \frac{a \cdot E^{1.75} + b - \text{BP}^{\text{scr}}}{c} \quad (3.10)$$

substituting all the constants we have:

$$\text{WET} = 1.165 \cdot \frac{0.002177 \cdot E^{1.75} + 0.9174 - \text{BP}^{\text{scr}}}{0.338} \quad (3.11)$$

where E is the initial energy of the beam, in MeV/u , and BP^{scr} is the BP position scored in the detector, i.e., expressed in channel number. The WET has units of millimeters. We can improve this equation by using the actual value for parameter c , i.e., $c = 1/3$, since this reflects the actual physical measurement of each PMMA slab and the value we got from the thickness calibration has a small error due to the method used. The final equation that will be used in this work is:

$$\text{WET} = 1.165 \cdot 3 \cdot (0.002177 \cdot E^{1.75} + 0.9174 - \text{BP}^{\text{scr}}) \quad (3.12)$$

CHAPTER 3. MATERIALS AND METHODS

As a verification of the simulation, a homogeneous PMMA cylinder with a diameter of 16 cm was irradiated with a ^{12}C ions beam with initial energy of 334.94 MeV/u. The beam energy has to be chosen such that the BP associated with zero thickness falls into the last few channels of the detector. If a slightly too high energy is selected, those BPs will fall beyond the detector impeding a proper detection. The irradiated field was 200 mm \times 10 mm with 1 mm steps in the x and y direction. The field irradiated the curved face of the cylinder. The simulation was run in the cluster (section 3.5) where 4800 primaries were transported per RP, i.e., 50 particles per RP in 96 threads of the cluster. These 96 outputs are independent and can be merged because different seeds were used for each thread, which results in statically independent simulations. The simulated data was then converted to PMMA equivalent thickness according to equation 3.12, but dropping the conversion factor from PMMA to water (1.165). Figure 3.8 shows the path length as a function of the lateral dimension. The simulated values (black dots) were plotted together with the known physical dimensions of the phantom (red line). It is easily seen that the simulated data agree quite well with the physical dimensions of the phantom. Again, the step like structure of the data is due to the fact that each channel of the detector has a finite nominal resolution of 3 mm of PMMA.

For thicknesses below 45 mm we see that some values were wrongly reproduced as zero, the black dots inside the area limited by the red line (black arrows in figure 3.8). This is due to the beam having a FWHM of 3 mm and traveling parallel to the interface PMMA/Air. And, as we approach the sides of the phantom, and since the phantom is cylindrical, less and less material is available to slow down the beam. This means that the majority of the particles, for these RPs, will travel through air instead of through the phantom, which will result in an average BP position in the zero WET channel.

Despite the small deviations due to the interfaces, this verification suggests the correctness of the conversion in PMMA equivalent thickness, or alternatively into WET using equation 3.12. The mean absolute error between the physical dimensions and the reconstructed values is ≈ 1.2 mm in PMMA.

After all the validations and calibrations we have all the conditions to use more complex phantoms, as will be shown in the following sections.

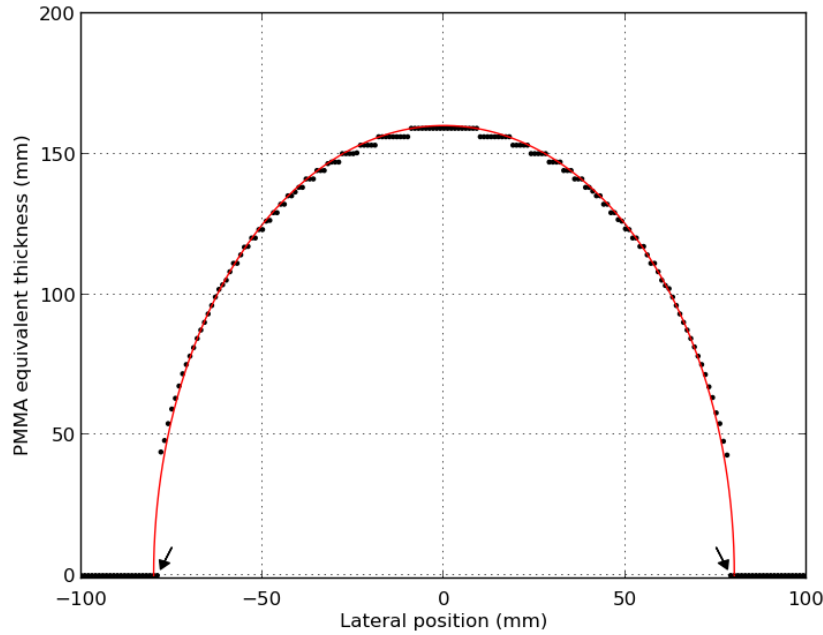


Figure 3.8: Projection of a simulated radiography of a homogeneous PMMA cylinder with 16 cm of diameter. The simulated values were converted to PMMA equivalent thickness. The simulated values (black dots) were plotted together with the know physical dimensions of the phantom (red line).

3.4 Digital phantom

In order to test the full capabilities of the simulation model, a more complex phantom was used. This phantom is a PMMA cylinder with five tissue equivalent rods: PMMA (1 rod), Air (2 rods), Lung (1 rod) and Cortical Bone (1 rod) and it is available at HIT. The physical dimensions of the phantom are presented in figure 3.9 as well as the position of the different rods. The PMMA cylinder has an height of 97 mm and the rods have an height of 70 mm.

Knowing the physical dimensions of the phantom and the equivalent WEPL of each material present in it (section 3.2.4), a perfect digital phantom was created using MATLAB. The WEPL values were measured at HIT and they are tabulated and used in the TPS.

The virtually defined phantom can have the resolution we desire. We started with a resolution of 2000×2000 pixels and then down sampled it to match the resolution of our simulated or experimental radiographies.

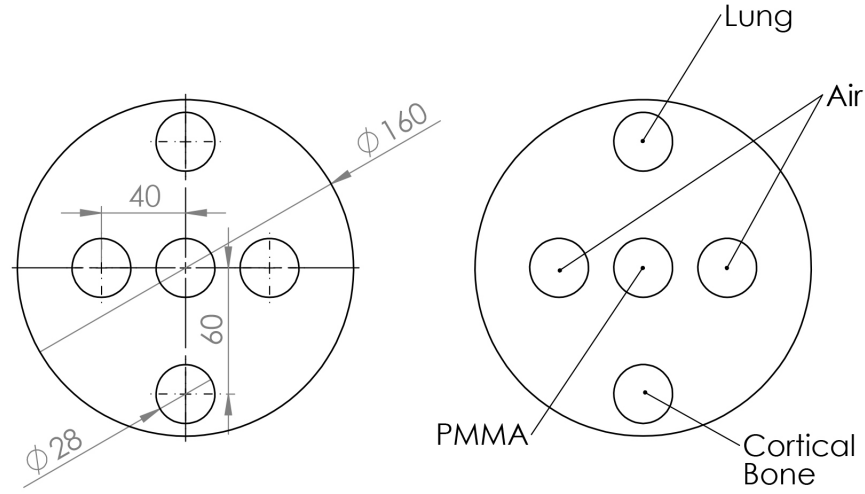


Figure 3.9: Top view of the PMMA cylindrical phantom with the physical dimension (left) and the position of the different rods (right). All dimensions are in mm.

From this digital phantom we can obtain a perfect radiography from every angle and also a perfect CT slice. We will use the phantom as the best possible scenario to compare our results with by, for example, calculating the root mean square error of a full radiography or CT. This will allow us to access the quality of the simulations and test different imaging approaches, e.g., changing the number of primaries per RP or the RP lateral separation and checking if the final result improves.

3.5 Compute cluster

MC simulations, depending on the complexity of the problem and how good we want the statistics to be, tend to take a long time to run. The time it takes also depends on the computing power available and the number of parallel jobs we can run.

For example, in order to simulate a slice of a ^{12}C Computed Tomography (cCT), where we scanned an horizontal line of 20 cm with 201 RPs (1 mm lateral stepping) and 400 primaries per RP, we need ≈ 30 min per projection. If we want to simulate 180 projections and we only have a single processor we need ≈ 90 hours which is ≈ 3.75 days. Fortunately, we have a compute cluster available that let us run parallel simulations.

The compute cluster used to perform all the simulations consists of 12 server nodes Fujitsu

CHAPTER 3. MATERIALS AND METHODS

PRIMERGY CX250. Each node has two 8 core Intel Xeon E5-2670 CPUs with 2.6 GHz (HyperThreading capable) and 64 GB RAM. In summary, the cluster consists of 192 CPU cores which means we can run up to 192 jobs in parallel. It also offers a queuing system that manages the jobs submitted to the cluster.

One way to speed up the cCT example above is to send a different simulation with a different projection to each node of the cluster. That way we can get up to 192 projections in 30 minutes.

For illustration, a bash script that runs 180 FLUKA jobs in the compute cluster can be consulted in appendix C.

Chapter 4

Results and discussion

4.1 Dose estimation

One of the main goals of this project is to optimize the carbon radiography and tomography so that the minimum dose is delivered to the patient while preserving acceptable image quality.

Starting from equation 2.3, a simplified version was proposed by (Krämer & Scholz, 2000) to estimate the dose for ion beam delivery when using a scanning system. Thus, the dose deposited in the patient can be approximated by:

$$D \approx \frac{N}{\Delta x \Delta y} \frac{1}{\rho} \frac{dE}{dx} \quad (4.1)$$

where D is the dose, N is the number of primaries per RP, Δx and Δy are the step size in the x and y direction, respectively, dE/dx is the stopping power and, finally, ρ is the density of the medium. Since we use the same energy for a full radiography and we are always overshooting the phantom, i.e, placing the BP outside of it, we can assume that the stopping power is slowly varying and the resulting plateau dose can be regarded in first approximation as a constant. From figure 4.1 we can see exactly this, the phantom (shaded in green) is entirely in the build up area of the Bragg curve which is relatively flat.

In order to test the approximation of equation 4.1, different simulations were performed using different energies, number of particles and different Δx and Δy stepping. A homogeneous PMMA cylinder with a diameter of 16 cm and an height of 2 cm was used as phantom. A scanning field of $18 \times 4 \text{ cm}^2$ was scanned to make sure that the whole phantom

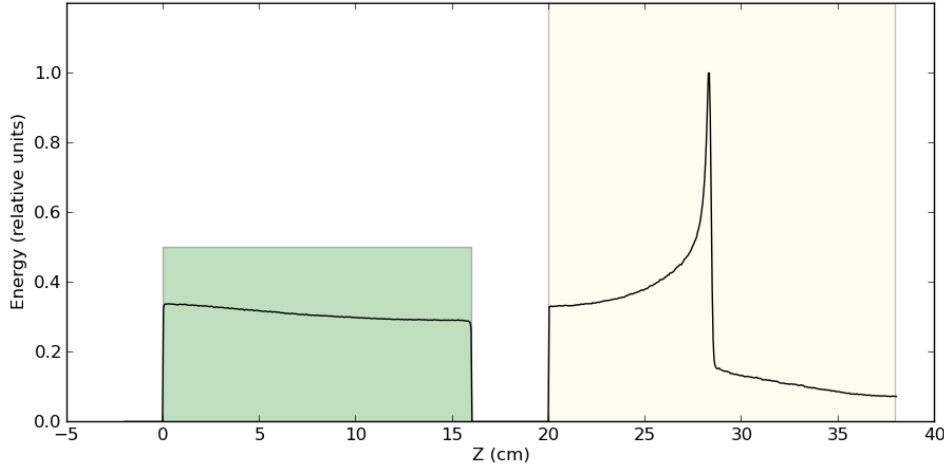


Figure 4.1: Depth dose deposition of a ^{12}C ion beam with initial energy of 409.97 MeV/u. The phantom, shaded in green, is an homogeneous PMMA cylinder with a diameter of 16 cm. The detector is shaded in yellow. The situation represents a central beam crossing the thickest part of the phantom.

was irradiated.

The dose was scored using the USRBIN card in FLUKA with the option Region activated. This option scores the total dose deposited inside a region, in this case, our phantom. FLUKA output has unit of $\text{GeV}\cdot\text{cm}^3/\text{g}/\text{p}$ and we had to multiply this result by the number of primaries and divide it by the volume of the phantom yielding GeV/g . Finally, to convert from GeV/g to $\text{J}/\text{kg} = \text{Gy}$, we had to multiply the value by the factor $1.602 \times 10^{-7} \text{ J}\cdot\text{g}/\text{kg}/\text{GeV}$. The results are shown in table 4.1.

The value of $1/\rho \cdot dE/dx$ is necessary for the estimation and we obtained it by shooting a ^{12}C ion beam at a water phantom and then scoring the depth dose distribution. We assume as the value for the $1/\rho \cdot dE/dx = dE \cdot S/dm$ the dose deposited in the first centimeter of the water phantom. This was repeated for all the energies used since the dE/dx depends on the initial energy of the beam.

From the results, we can observe that the estimation of equation 4.1 overestimates the dose deposited in the phantom up to $\approx 15\%$ which can be seen as a safety margin. From now on, all the dose values presented in this thesis will be estimated using equation 4.1. The results also show that, as expected, the dose increases linearly with the number of particles per RP and decreases quadratically with increasing the lateral and vertical stepping, as

Average dose deposited in the phantom

Energy (MeV/u)	$\frac{1}{\rho} \frac{dE}{dx}$ (GeV.cm ² /g)	# primaries	$\Delta x = \Delta y$ (cm)	Simulation (mGy)	Estimation (mGy)
334.94	0.12062	2500	0.1	4.58	4.83
			0.2	1.14	1.21
		5000	0.1	9.16	9.66
			0.2	2.29	2.42
353.76	0.11721	2500	0.1	4.31	4.69
			0.2	1.08	1.17
		5000	0.1	8.61	9.39
			0.2	2.15	2.35
409.97	0.10650	500	0.1	0.76	0.85
			0.2	0.19	0.21
		1500	0.1	2.28	2.56
			0.2	0.57	0.64
		5000	0.1	7.59	8.53
			0.2	1.90	2.13
			0.3	0.84	0.95
			0.4	0.48	0.53
			0.5	0.30	0.34
			0.6	0.21	0.24
430.10	0.10674	2500	0.1	3.67	4.27
			0.2	0.92	1.07
		5000	0.1	7.27	8.55
			0.2	1.82	2.14

Table 4.1: Average dose deposited in the phantom for different settings of the radiography

shown in figure 4.2. For example, increasing the lateral stepping x and y from 1 mm to 2 mm will reduce the deposited dose by a factor of 4, while decreasing the number of particles from 2500 primaries to 1250 will reduce the deposited dose only by a factor of 2. Finally,

CHAPTER 4. RESULTS AND DISCUSSION

we see that using higher energies, for the same stepping size and number of primaries, the deposited dose decreases slightly, as shown in table 4.1. This is due to the decrease of the dE/dx as we increase the initial energy of the beam.

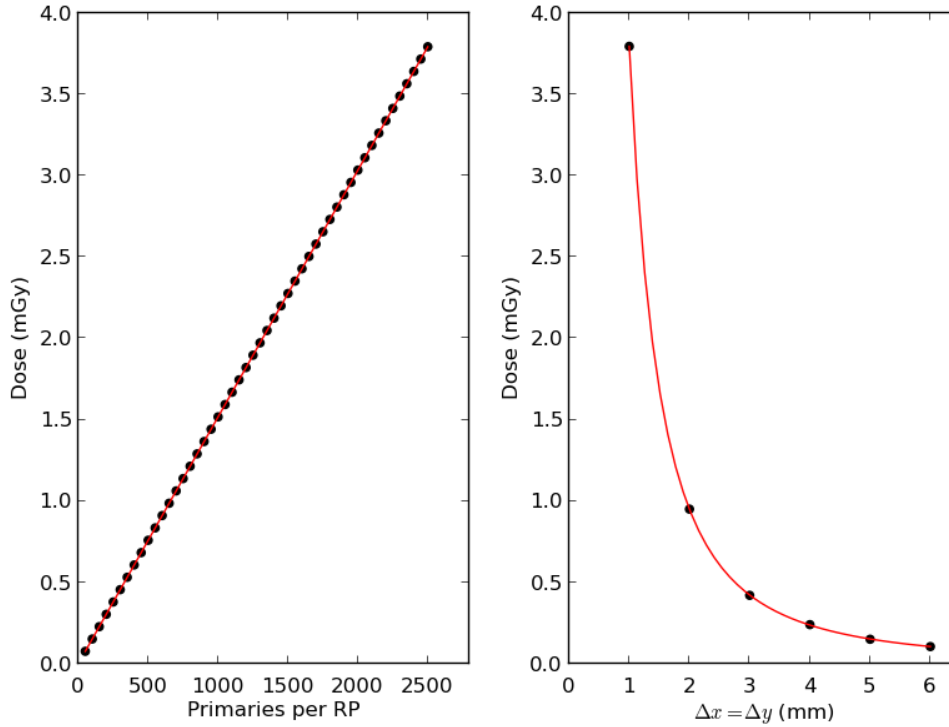


Figure 4.2: Dose deposited in the phantom for different number of primaries (left) and for different lateral and vertical scanning step size (right). The simulation data (dots) was fitted (lines) with a linear fit (left) and with an inverse quadratic fit (right).

4.2 Simulated carbon ions radiography

In this section we will consider simulations of carbon ion radiographies of the cylindrical phantom with inserts (section 3.4) using different settings. The purpose is to optimize the radiography process, i.e., find a compromise between image quality and dose deposited in the phantom. We should make it clear that all radiographies result from irradiating the phantom from its side, the curve side of the cylinder.

The first step was to correctly design our phantom in FLUKA, using the actual dimensions

CHAPTER 4. RESULTS AND DISCUSSION

of the phantom (see section 3.4). This was achieved by using the Geometry Editor available in FLAIR. The final result can be seen in figure 4.3.

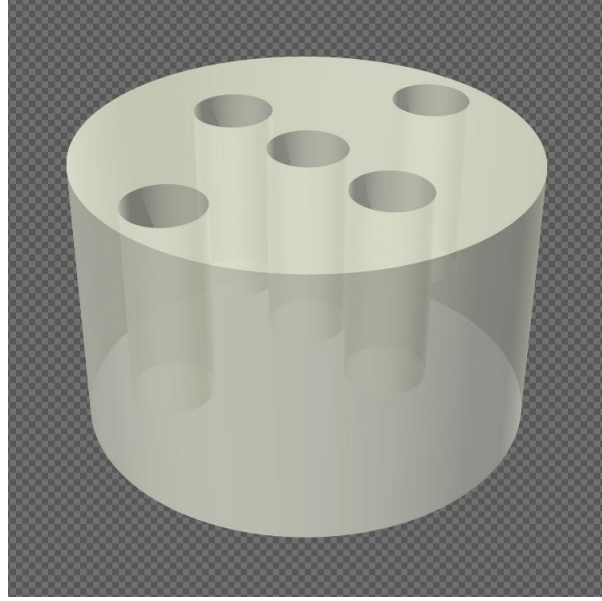


Figure 4.3: PMMA cylindrical phantom with inserts implemented in FLUKA. Transparency is added to show the inside of the phantom.

The next step was to simulate a radiography of the phantom using FLUKA and then import and process the data using the self-written MATLAB routines. For the simulation, the phantom was irradiated with a lateral field of $200 \text{ mm} \times 26 \text{ mm}$ and Δx and Δy steps of 1 mm. The beam had an initial energy of 334.94 MeV/u and 2500 primaries were transported per RP. Figure 4.4 shows a comparison between the true, the simulated and the experimental radiography (Rinaldi et al., 2014). The true radiography was obtained directly from the digital phantom (section 3.4). The experimental radiography and the simulated one share the same method but, for the experimental radiography 5000 primaries per RP were used. We should state that this number reflects the experimental detection efficiency, which is much lower than what we have with the simulations (Rinaldi et al., 2014).

As we can see, the three radiographies look similar but, for the experimental one, some artifacts are visible due to electronic noise, wrong detection of the BP or simply malfunctioning channels of the detector.

We also compare a central section in the x direction from the radiographies (figure 4.5), showing that the simulated radiography agrees quite well with the true case, although it

CHAPTER 4. RESULTS AND DISCUSSION

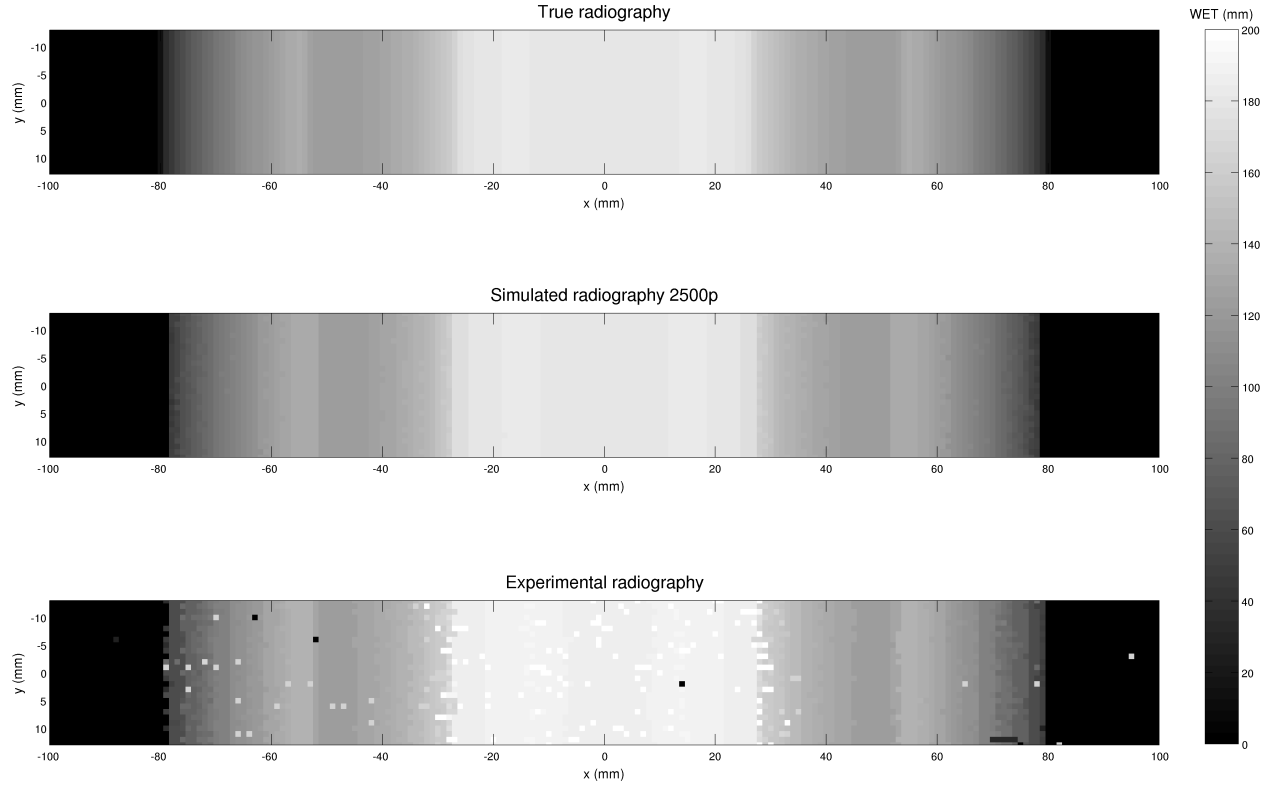


Figure 4.4: Comparison of radiographies of the cylindrical phantom with inserts.

also exhibits a step-like structure while the true data is smooth. For the experimental data, the step-like structure is also present, but there is an overestimation of the WET for higher depths and outside of the phantom, where negative WET values instead of zero are found. Additionally, some spikes are seen due to experimental errors in BP identification and the technical issues already mentioned.

In order to minimize the dose delivered to the phantom, we investigated scenarios with lowered number of particles per RP and accessed the Normalized Root Mean Square Error (NRMSE) of each radiography when compared to the true case. The Root Mean Square Error (RMSE) of predicted values \hat{y}_t for times t of a regression's dependent variable y is computed for n different predictions as the square root of the mean of the squares of the deviations:

$$\text{RMSE} = \sqrt{\frac{\sum_{t=1}^n (\hat{y}_t - y_t)^2}{n}} \quad (4.2)$$

The NRMSE is given by normalizing the RMSE by the range of observed values of the

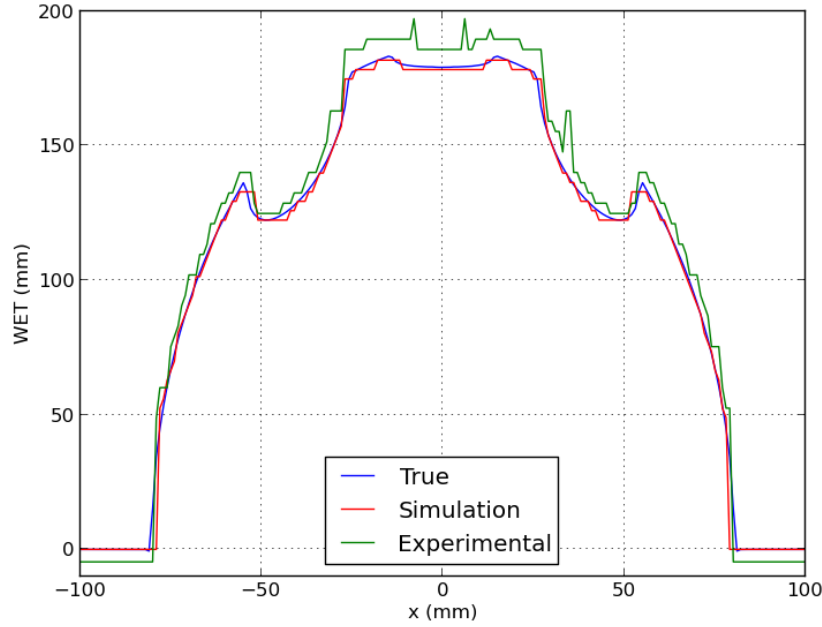


Figure 4.5: Comparison of the central section in the x direction from the radiographies shown in figure 4.4.

variable being predicted:

$$\text{NRMSE} = \frac{\text{RMSE}}{y_{\max} - y_{\min}} \quad (4.3)$$

this value is often expressed as a percentage, where lower values indicate less residual variance (Devore & Berk, 2011).

In our case, the true radiography is the observed values, y , and the simulated radiography the predicted ones, \hat{y} . The calculation is made point by point, i.e., each pixel is a different t and n is the sum of all pixels in one image.

Figure 4.6 shows the degradation of the image when we lower the number of particles and in table 4.2 we have the dose delivered to the phantom and the correspondent NRMSE for different number of particles.

Finally in figure 4.7 we have a plot showing how the NRMSE changes with different number of particles. From the figure and from table 4.2 we can conclude that more than 100 particles per RP will not improve the image quality since the NRMSE is relatively constant after that value. Increasing the number of particles will just increase the dose deposited in the phantom.

CHAPTER 4. RESULTS AND DISCUSSION

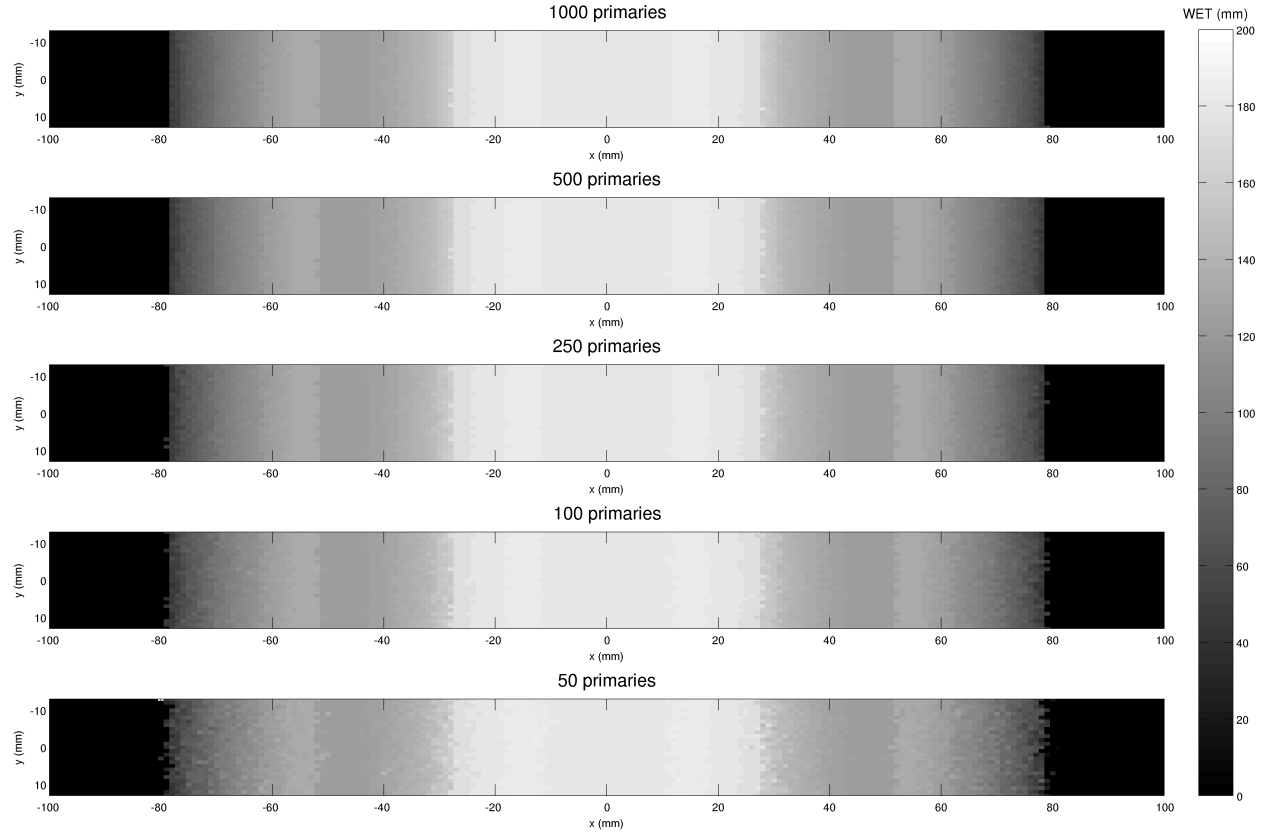


Figure 4.6: Simulated radiography for the same configuration with different number of primaries per RP.

We should also notice that each pixel in the image corresponds to one RP in the simulation and in the experimental radiography, and that the spatial resolution is related with the lateral beam size and not with the lateral scan stepping. This being said, using smaller and smaller steps will not increase the spatial resolution since our beam, with the energy used, has a FWHM of 3.7 mm. Using smaller steps will increase the dose deposited in the phantom without improving the image quality.

The 1 mm stepping was chosen since, in order to obtain a homogeneous field, (Krämer & Scholz, 2000) suggested the use of a stepping size of:

$$\Delta x = \Delta y \leq \frac{1}{3} \times \text{FWHM} \quad (4.4)$$

which results in a stepping of ≈ 1.2 mm for the beam energy used. We also know that this

NRMSE and deposited dose

Primaries	NRMSE (%)	Dose (mGy)
25	5.1	0.05
50	2.5	0.10
100	2.3	0.19
250	2.2	0.48
500	2.2	0.97
1000	2.3	1.93
2500	2.2	4.83

Table 4.2: Dose deposited in the phantom and NRMSE for the same radiography settings but different number of simulated primaries per RP

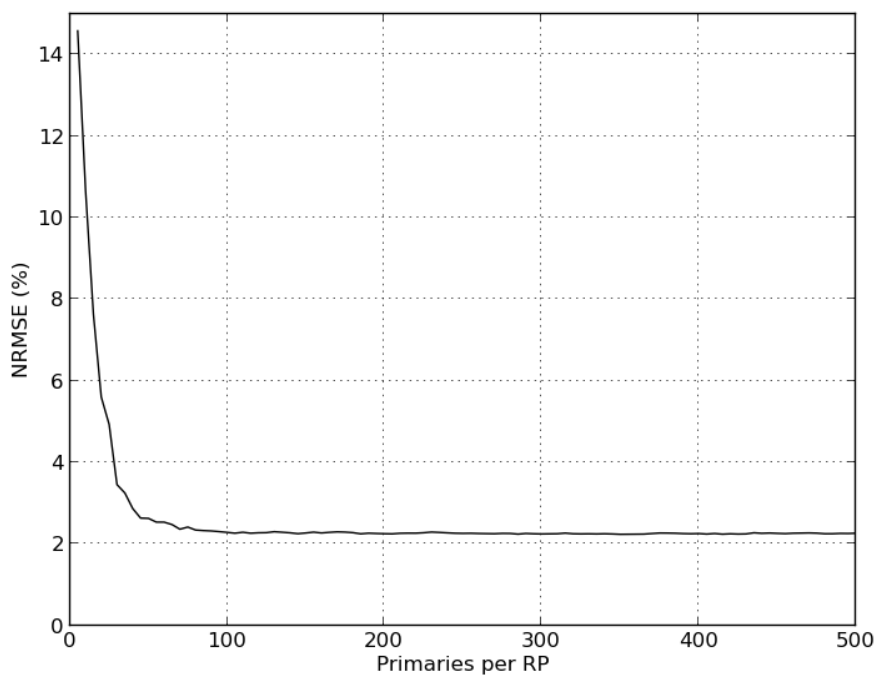


Figure 4.7: NRMSE for different number of particles. The curve resulted from averaging 3 completely independent runs of the same radiography.

CHAPTER 4. RESULTS AND DISCUSSION

equation is very conservative and for that reason we investigated bigger stepping sizes.

In pursuing that purpose, we evaluated the homogeneity of lateral dose profiles when using different lateral stepping sizes. The results are illustrated in figure 4.8, and we can see that using a lateral stepping of 2 or even 3 mm results in a dose homogeneity similar to what is achieved using 1 mm with mean values within $\approx 0.2\%$ and $\approx 0.9\%$ as well as comparable standard deviation. For 4 mm lateral stepping we can no longer consider the dose field homogeneous, as we can also see from the figure and the corresponding obtained values.

It should be reminded that, using these bigger stepping sizes will reduce the dose deposited in the phantom without, in principle, reducing the image quality. To test this last statement, the radiography of our phantom was repeated, this time with a lateral stepping of 2 mm. The results are shown in figure 4.9, and comparing the true radiography obtained from the virtual phantom with the radiography from the simulation with 500 ions per RP, we achieve a NRMSE of 2.2%. This value is consistent with the values from the 1 mm stepping radiographies, (cf. table 4.2), and it proves that the information from the radiography with 1 mm stepping is quite similar with the information we obtain when using 2 mm stepping. For a radiography with 3 mm stepping the resulting NRMSE is 4.0%.

As said earlier, the image resolution is related to the size of the beam and not with the lateral stepping, assuming that the dose distribution is homogeneous. Hence, 1 mm lateral stepping will result only in oversampling, yielding only increased dose without a corresponding quality improvement of the radiography.

The radiography with 2 mm stepping uses fewer raster points than the one with 1 mm stepping. This results in a final image with approximately half the pixels of the radiography with 1 mm stepping because, when reconstructing the image, we attribute one pixel in the image to each RP. For this reason, the next step is to make the image size independent of the number of raster points irradiated as well as to include the beam shape into the image reconstruction algorithm.

We started by creating a binning grid with $0.5 \times 0.5 \text{ mm}^2$ pixels. Then, since we know the shape of the beam from the MC simulations, we can use this information in the reconstruction algorithm to improve the quality of the radiography. Figure 4.10 shows a pencil beam fluence map that was converted to a cumulative distribution by dividing all the values by the integral of the distribution. This means that, a single particle in the beam has a certain probability of

CHAPTER 4. RESULTS AND DISCUSSION

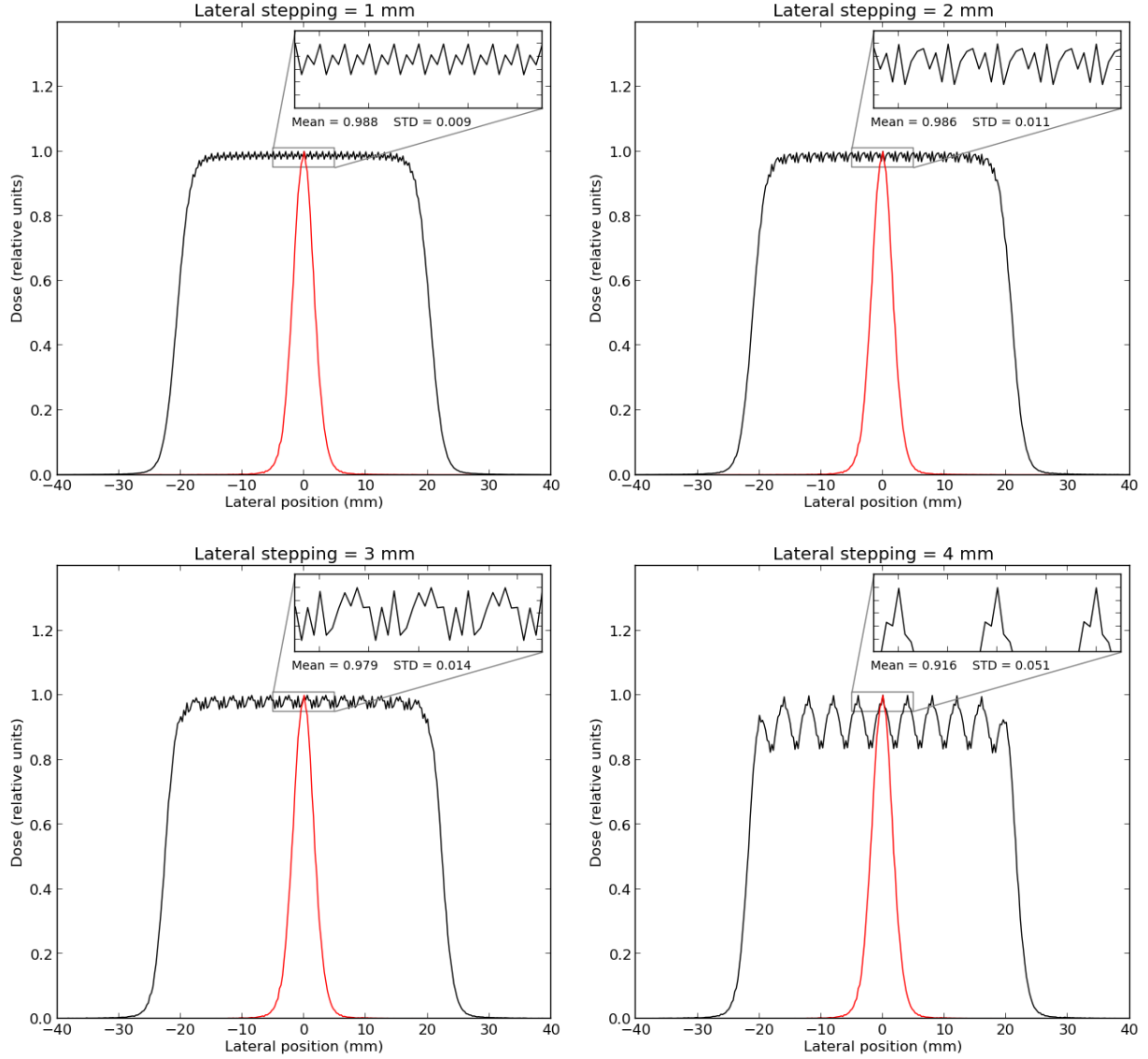


Figure 4.8: Comparison between lateral dose profiles when using different lateral stepping sizes. In red we have the lateral profile of a single beam spot and in black the resulting extended lateral profile. A zoom of the area of interest is shown and the mean and the standard deviation of that area is calculated.

being in a certain position according to this map. In order to include this information in the radiographic image formation, we randomly sample different particle positions, according to this map, belonging to one RP, and assign to them the WET simulated for this RP. Then, we add the WET values to the bin where these particles belong and repeat this process for all the RPs. Finally we divide the cumulative WET in each bin by the number of particles

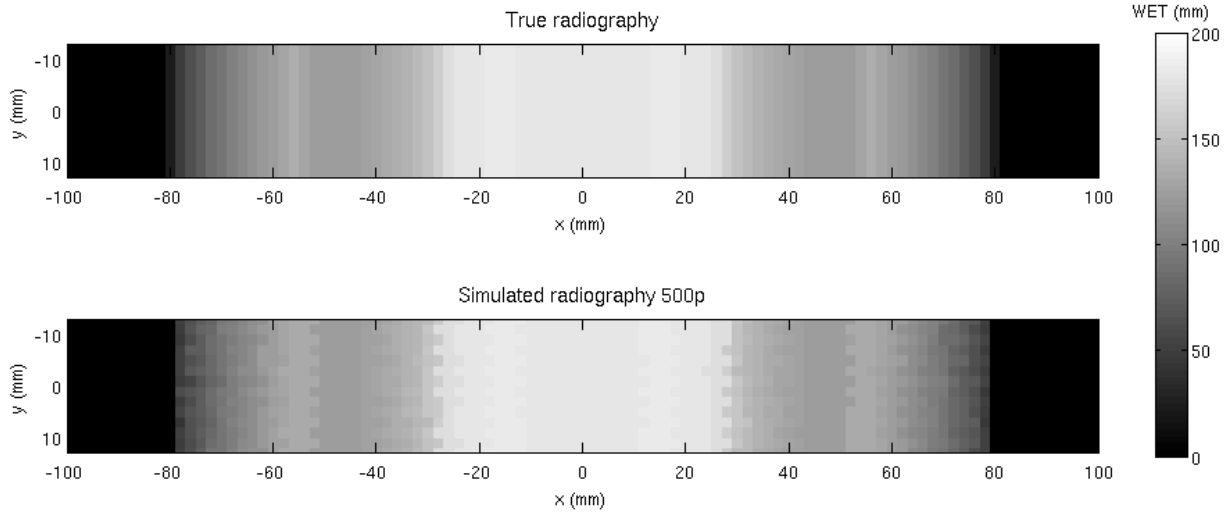


Figure 4.9: Comparison between the true radiography of the cylindrical phantom with inserts and the simulation for 500 ions per RP. The lateral stepping used was 2 mm.

that went inside that bin resulting in our reconstructed radiography.

The radiographies reconstructed with this new algorithm can be seen in figure 4.11. The first feature we notice is the smooth transition at interfaces, where the image no longer presents the artifacts that were seen, for example, in figure 4.9 around $x = -3$ cm and $x = 3$ cm. These artifacts appeared because the images are produced from the detector by assigning to each RP a unique channel number. If two BPs are present in the signal, both contain information on the densities of the irradiated volume in the region around the beam axis defined by the beam width, but we were ignoring this information when identifying the position of only one of the BPs. Since we need to have some overlap of RPs in order to achieve an homogeneous dose field (cf. figure 4.8), we can use the available information of the finite beam size in the image formation process. Now, our algorithm includes the beam shape and each bin in the image can receive contributions from different RPs which is expected to improve the quality of the final image.

The last step is to compare radiographies reconstructed with this new algorithm and the previous one when obtaining radiographies with only 100 particles per RP and with 1 mm, 2 mm and 3 mm lateral and vertical stepping as shown in figure 4.11. With the new method we managed to reduce the NRMSE from $\approx 2.2\%$ to 1.1% and 1.2% for the 1 and 2 mm stepping, respectively. This allows us to conclude that the new reconstruction algorithm is able to increase the quality of the images for the case of 1 mm and 2 mm lateral stepping

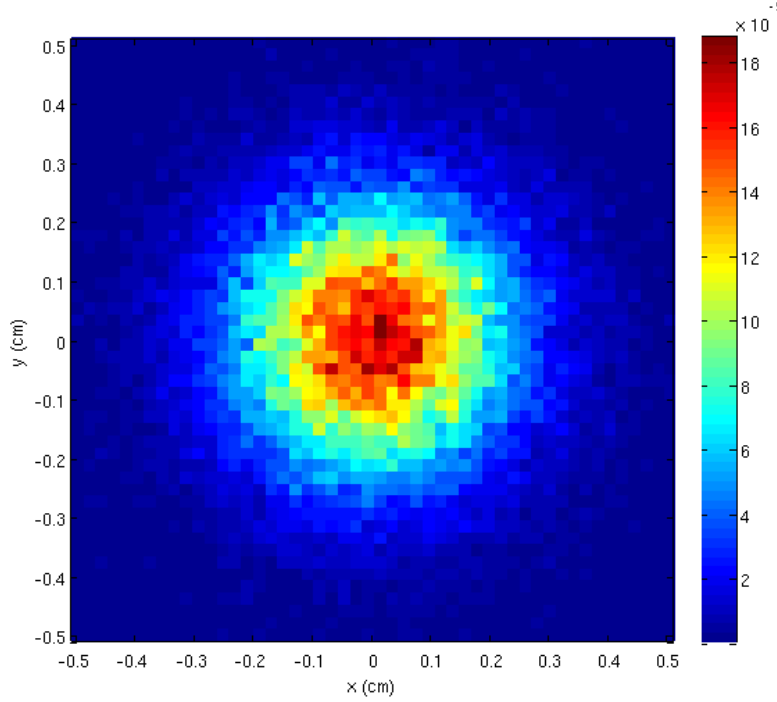


Figure 4.10: Cumulative distribution of the beam as obtained from the MC simulation. The x and y position of a single particle in the beam is randomly sampled according to this distribution. The beam shape can also be recognized.

size.

The NRMSE for the 3 mm radiography reduced from 4.0% to 2.6% but some visible artifacts, specifically waving shapes, can be seen in the radiography. This affect is ascribed to the stepping being too large, indicating that the results for this lateral and vertical stepping are not satisfactory.

The best results are produced by the 1 mm and 2 mm stepping radiographies since both have equivalent NRMSE of 1.1% and 1.2%, respectively. However the dose deposited for the 2 mm radiography is ≈ 4 times smaller than the dose deposited for the 1 mm one, with values of 0.05 mGy and 0.18 mGy, respectively. This allows us concluding that the increase in dose is not worth the slightly better radiography.

In figure 4.12 we can see a comparison of the WET values for a vertical section of the radiography with 1 and 2 mm stepping in a non-interface region, $x = 0$ mm, and in an interface region, $x = -30$ mm. We also show the use of *a priori* beam information. Since our phantom is homogeneous in the y dimension a constant WET value was correctly

CHAPTER 4. RESULTS AND DISCUSSION

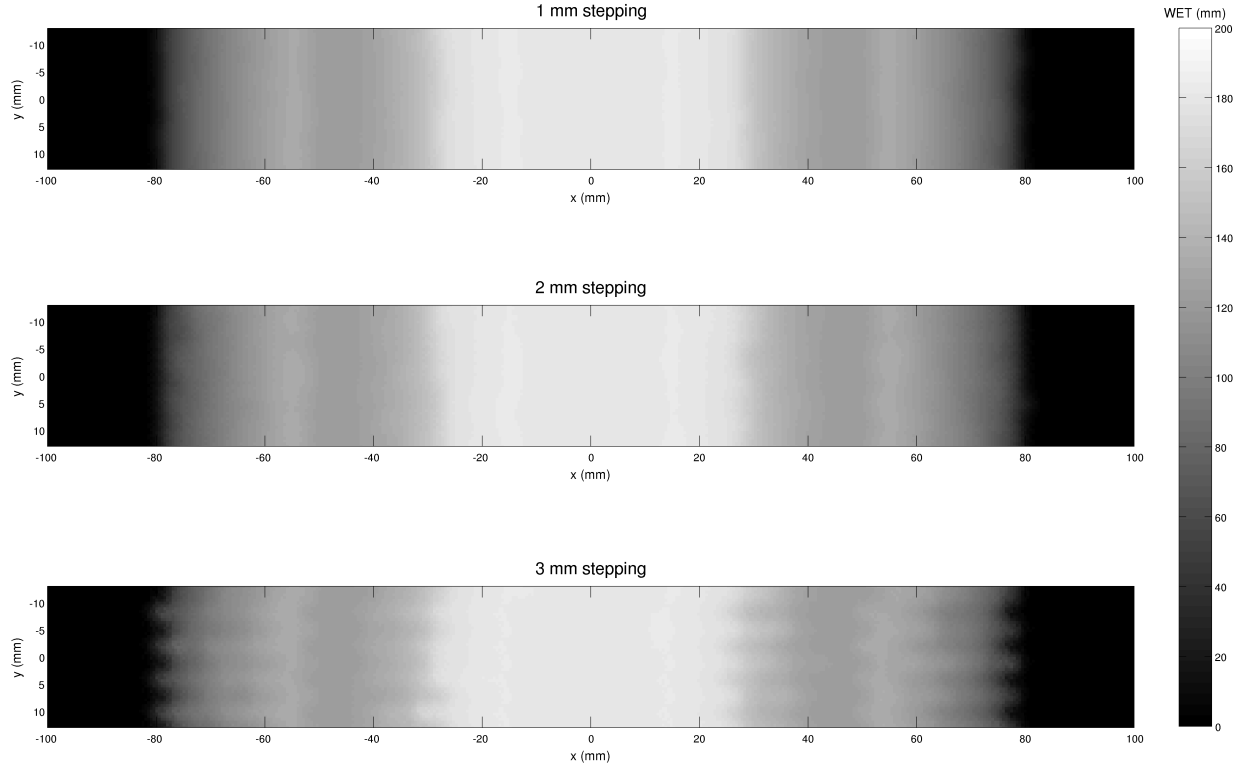


Figure 4.11: Comparison between the reconstructed radiographies with the new algorithm. The different lateral and vertical stepping used were 1 mm, 2 mm and 3 mm for the same low number of 100 ions per RP.

reconstructed for the non-region interface. Once again, the WET values do not match exactly the true one due to the finite depth resolution of 3 mm of our detector. This resolution could be improved with methods that virtually increase the nominal range of the detector, as suggested in (Rinaldi, 2011). For the interface region the homogeneity of the phantom in the y dimension is not correctly reproduced since we can see some oscillations in the WET values. Some spikes are clearly visible when no *a priori* information is used. Although including the beam shape *a priori* information in the reconstruction algorithm improved the image quality, it did not fix completely the interface problem.

Now that the radiography process is optimized, we can repeat it for different projections of the phantom and reconstruct a simulated cCT.

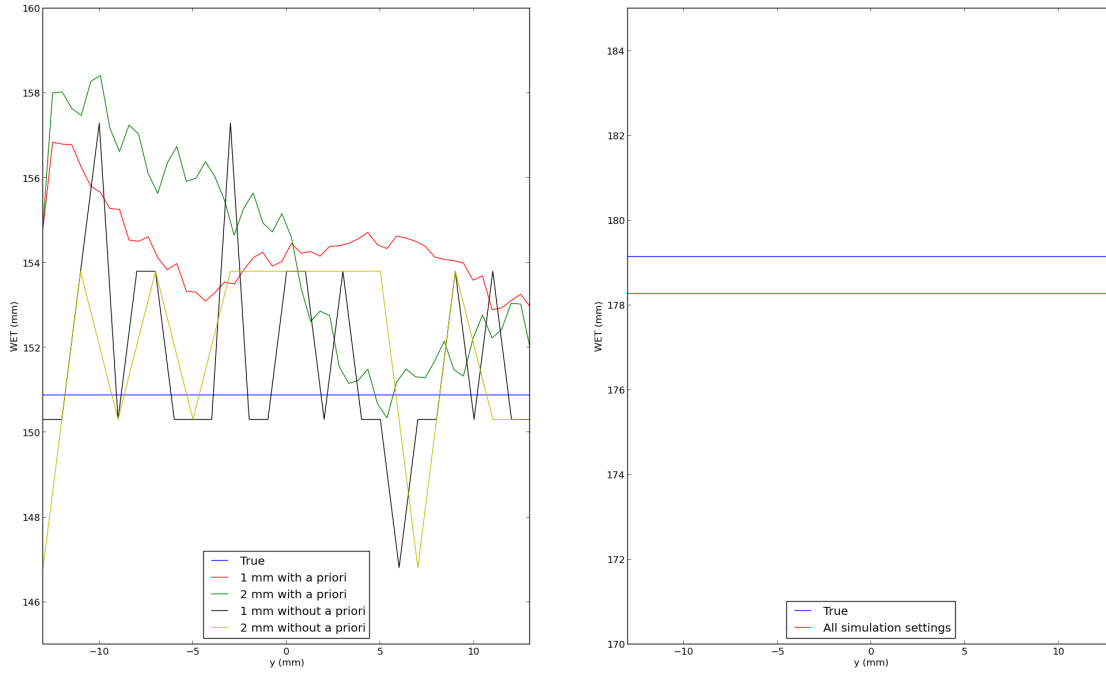


Figure 4.12: Comparison between a vertical section of the 1 mm and 2 mm stepping radiography in a non-interface region, $x = 0$ mm (right), and in an interface region, $x = -30$ mm (left). The true value is also shown. We also evaluate the use of *a priori* information in the reconstruction.

4.3 Simulated carbon ion tomography

As a proof of principle, a tomographic reconstruction of the cylindrical phantom was performed. We started by using the FLUKA ROT-DEFini card to rotate our phantom around its center in the clockwise direction when seeing it from the top, as shown in figure 4.13. Then, we created different simulations with a different number of projections of the phantom, i.e., we scanned the same extended field for every rotation angle of the phantom. The radiographies were obtained with a ^{12}C beam of 334.94 MeV/u through a horizontal scanning line (x direction) of 20 cm. We used a lateral stepping of 1 mm and 2 mm, we shot 100 primaries per RP and applied the same algorithms as explained in section 4.2. Again, these radiographies irradiated the curve side of our cylindrical phantom. Each projection is similar to a central section of the radiography from figure 4.11. Finally, we obtained 3 sinograms for each stepping, one with 181 projections, one with 361 and the last one with 721, all equi-spaced angles between 0° and 180° , i.e., in 1.00° , 0.50° and 0.25° steps,

CHAPTER 4. RESULTS AND DISCUSSION

respectively. Since carbon ions travel almost in a straight line, we can see this as a parallel-beam tomography problem which means that we only need to irradiate 180° of the phantom since the other 180° will have symmetric information.

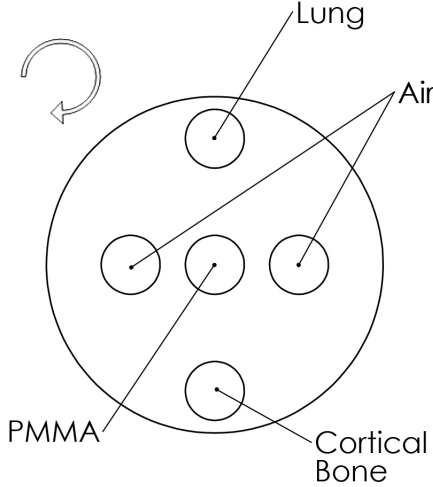


Figure 4.13: Top view of the PMMA cylindrical phantom showing the rotation direction for the tomography.

We started by reconstructing the image with a filtered backprojection algorithm from MATLAB, *iradon* function, which uses a spline interpolation for the backprojection and a Hann filter, a Ram-lak filter multiplied by an Hann window, for the filtering. Then, we compared the results with the true phantom and obtained a NRMSE of 7.0% for both 181 and 361 projections and a NRMSE of 6.9% for the reconstruction with 721 projections. The dose deposited in the phantom was 8.75 mGy, 17.47 mGy and 34.89 mGy, respectively. These initial results suggest that using more than 181 projections does not improve the quality of the reconstruction while the dose increases linearly with the number of projections. For this reason, we decided to reconstruct the image with more sophisticated algorithms based on iterative methods.

We used the AIRtools package, a MATLAB package of algebraic iterative reconstruction (Hansen & Saxild-Hansen, 2012). The used routine implements a Simultaneous Algebraic Reconstruction Technique (SART) algorithm as explained in (Andersen & Kak, 1984). In figure 4.14 we have the true CT and the reconstructed one from the sinogram with 361 projections. We can see that the phantom was correctly reconstructed and we can distinguish

CHAPTER 4. RESULTS AND DISCUSSION

all the different tissue rods. Some line artifacts are present in the image due to the finite size of the beam and the interface problem that arises from that.

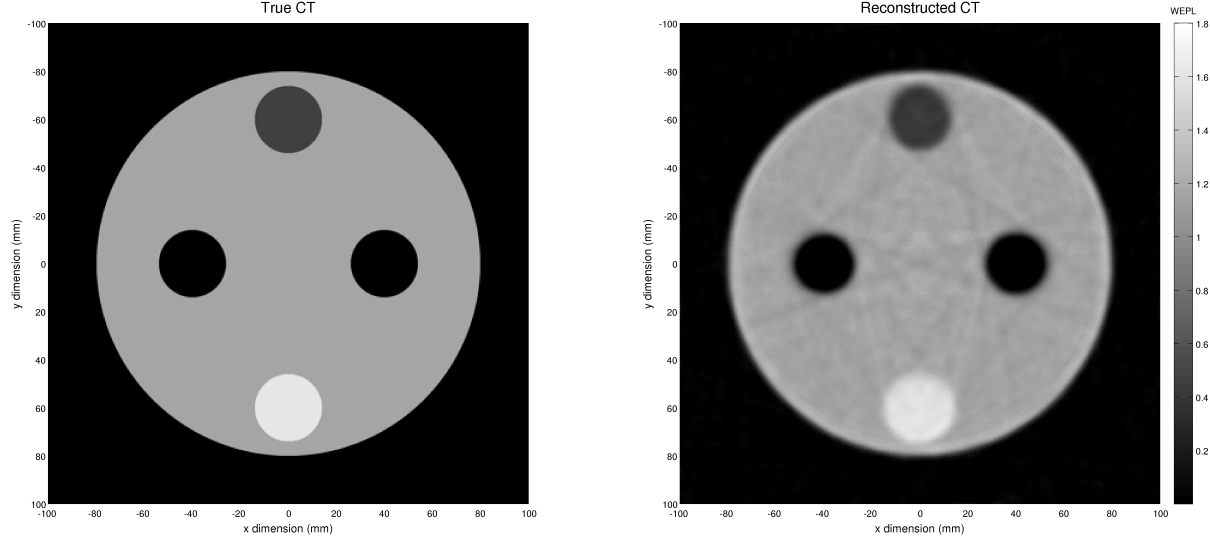


Figure 4.14: Comparison between the reconstruction (right) of the cylindric PMMA phantom with rods using a SART algorithm with 361 projections and the true one (left). A 2 mm lateral and vertical step size was used.

In figure 4.15 we can see two central sections of the CT image, one in the horizontal direction and another in the vertical direction. The reconstructed values roughly reproduce the expected WEPL of the different materials. The NRMSE for the full CT was 5.4% for the 181 and 361 projections and 5.3% for the one with the 721 projections. These reduced values show that using an iterative method can improve the image quality. We should also notice that there was no clear improvement in the image quality when increasing the number of projections above 181, similar to what we concluded using the filtered backprojection.

In order to test if the *a priori* beam information would improve the CT quality as it did with the radiography (section 4.2), we compared the same 361 projections reconstruction with 1 mm stepping and 100 primaries per RP with and without this reconstruction phase (figure 4.16). The *a priori* information reduced the noise from the image and the white ring artifact around the phantom. The NRMSE also decreases from 8.0% to 5.4% which show that there are advantages in including this *a priori* information. In figure 4.17 we have two central sections of the CT image and we can see that using *a priori* information reduces the noise of the image and reduces the spikes around the edges of the phantom.

CHAPTER 4. RESULTS AND DISCUSSION

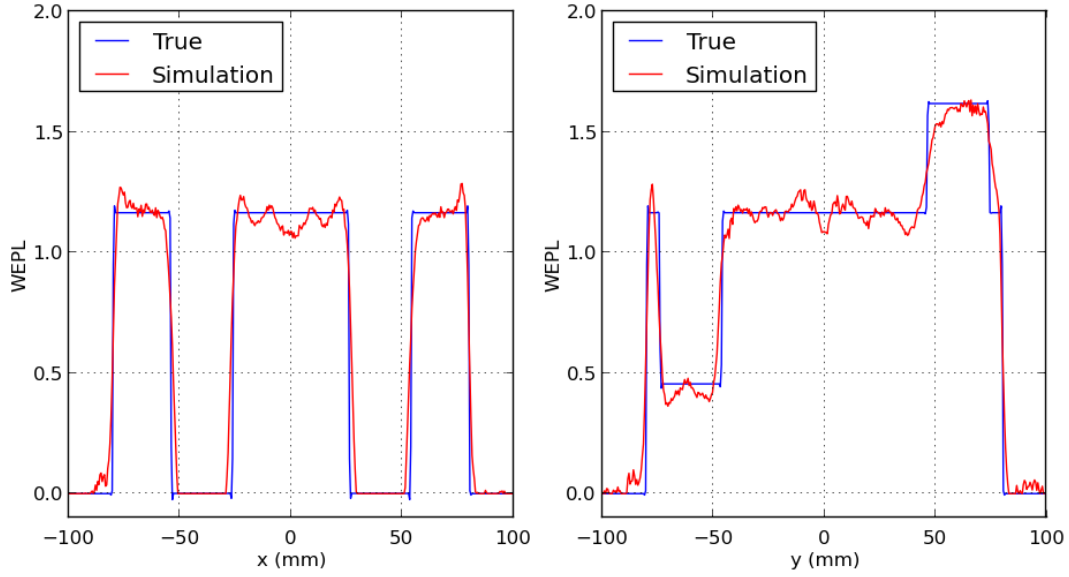


Figure 4.15: Central sections in the horizontal (left) and vertical direction (right) of the reconstructed CT and the true one.

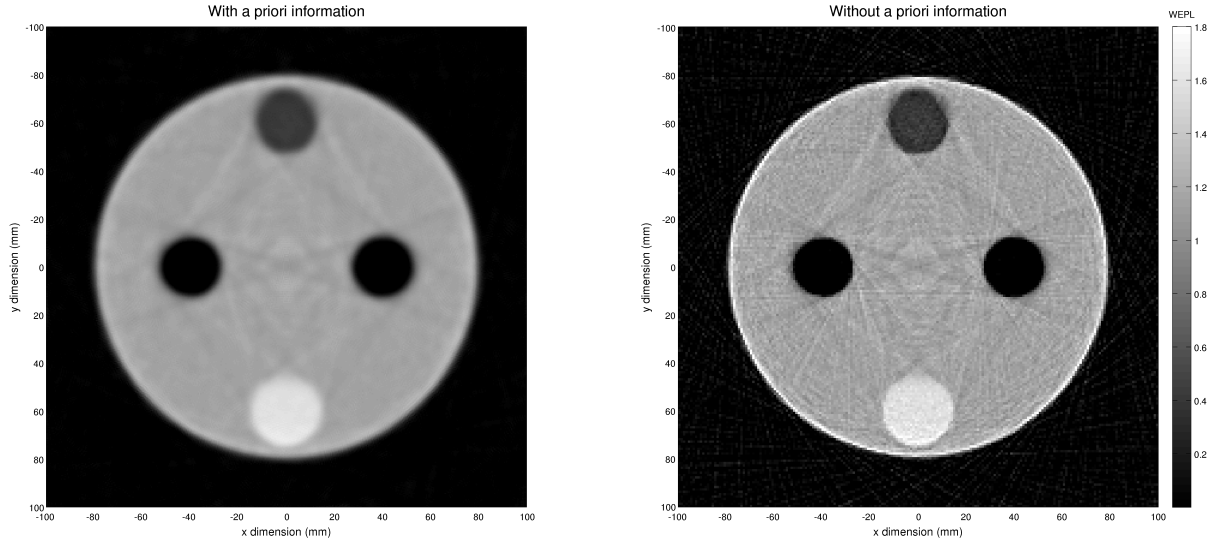


Figure 4.16: Comparison between the same reconstruction with (left) and without (right) *a priori* beam shape information. These images result from a 361 projections SART reconstruction, 1 mm lateral stepping and 100 particles per RP.

CHAPTER 4. RESULTS AND DISCUSSION

We should state that the NRMSE for the 1 mm lateral stepping CT and for the 2 mm one is the same, 5.4%, which shows that there is no advantage in using this smaller stepping size. These results agree with what was found for the radiography process.

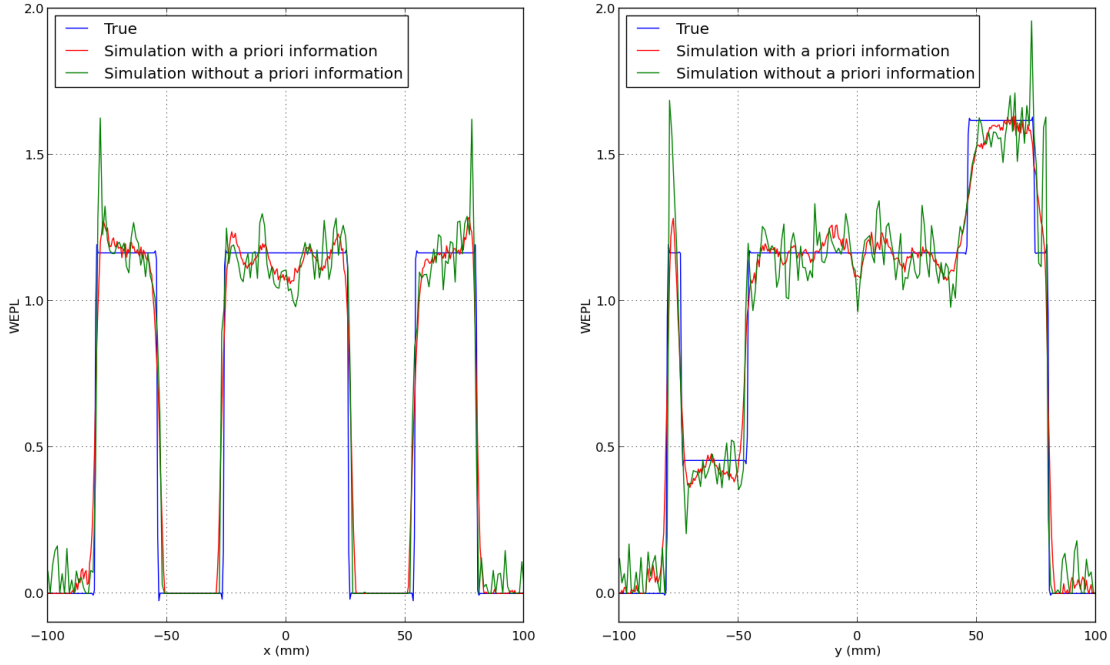


Figure 4.17: Central sections in the horizontal (left) and vertical direction (right) of the reconstructed CT with and without *a priori* information and the true one.

Finally, the dose deposited for the 2 mm stepping size scenarios is below the 50 mGy limit suggested by (Schulte et al., 2004) for a ion computed tomography system. Also, for the 181 and 361 projections, the dose deposited is compatible with what is clinically done today with X-rays. We should also state that X-rays CT gives us only HUs which then have to be translated into WEPL. This conversion has known limitations especially in plastic tissue-equivalent materials (see section 2.4).

Chapter 5

Conclusion and Outlook

Imaging techniques play a crucial role in treatment planning and range verification for ion beam therapy. In this thesis, a Monte Carlo study was carried out in order to support the imaging performance of a prototype detector for carbon ion radiography and tomography.

A simulation framework based on FLUKA was developed. The beam line from Heidelberg Ion Therapy Center (HIT) was reproduced as close as possible by including phase space files with the properties from 20 million particles in the simulation. The model is also capable of scanning a particle beam over an extended field and output a Bragg Curve (BC) with the depth resolution of the prototype detector for each individual Raster Point (RP).

The computational framework was calibrated and validated against experimental data and a good agreement between the simulation results and the available experimental data was achieved. This showed that the developed Monte Carlo model is a reliable tool to investigate details related to ion transmission imaging applications, that are difficult or time consuming to explore experimentally.

After this initial validation, different radiographies of a PMMA cylindrical phantom with inserts were performed. The purpose was to investigate different radiography settings and infer information about the image quality and the dose deposited in the phantom. Low dose radiographies were obtained while yielding realistic and reproducible results. Also, the imaging formation algorithm was upgraded in order to include *a priori* information of the beam shape.

After the radiography process was optimized, we decided to investigate Heavy Ion CT (HICT). Tomographic images were reconstructed based on radiographies, where each pro-

CHAPTER 5. CONCLUSION AND OUTLOOK

jection of the sinogram was a radiography of the phantom at a different angle. We showed that it is possible to obtain a good quality ^{12}C Computed Tomography (cCT) image while depositing in the phantom a dose equivalent to what is clinically done today with X-rays CT. All the results, for the radiographies and for the CT, were compared with a digital version of the phantom used. From our results in our ideal simulated conditions, we recommend a 2 mm lateral stepping size, 100 primaries per RP and the use of *a priori* beam information to achieve the best ratio between dose and image quality for the radiography. For a cCT, we recommend the same settings as for the radiography and the use of 181 projections.

Summarizing, the results of this study strongly support cCT as very promising imaging modality which could help reduce range uncertainties in ion therapy by performing the planning CT with the particle that is used to treat the patient. This will allow us to obtain valuable treatment information on the patient-specific stopping properties for indirect *in-vivo* range verifications. Also, low dose imaging guidance at the treatment site could be possible.

But, there is still a long way to go before this can be achieved. For the future, the analysis performed in this thesis should be repeated with more complex phantoms in order, e.g., to find the spatial resolution of the radiographies. This can be done by using a phantom with lines and evaluate the number of lines that we can distinguish. Right now, the spatial resolution is limited by the physical dimensions of the beam but single particle tracking detectors with single particle energy resolution could improve it. We should notice that this tracking would result in a more complex and expensive system than what we have. On the software side, in this thesis we only tested filtered backprojection and SART algorithms for the cCT reconstruction, which are algorithms that are not optimized for the application presented here. Other reconstructions algorithms could be tested to infer which one would give the best results. Also, a software interface was created in order to use our simulated sinograms in an image reconstruction code developed by collaborators from the Aarhus University in Denmark. This code, developed especially for proton tomography, is expected to improve the image quality we can achieve. Finally, all the findings have to be applied to the experimental setup, which will surely involve solving technical problems that are not present in the simulation world.

Another Masters student will replace me and continue working on this project. He will keep using and improving the Monte Carlo tools developed in this thesis.

References

- Andersen, A. H., & Kak, A. C. (1984). Simultaneous algebraic reconstruction technique (SART): a superior implementation of the ART algorithm. *Ultrason Imaging*, 6(1), 81–94.
- Barkas, W. H. (1963). *Nuclear Research Emulsions*. Academic Press.
- Battistoni, G., Muraro, S., Sala, P., Cerutti, F., Ferrari, A., Roesler, S., et al. (2007). The FLUKA code: Description and benchmarking. In (Vol. 896, pp. 31–49).
- Bauer, J., Sommerer, F., Mairani, A., Unholtz, D., Farook, R., Handrack, J., et al. (2014). Integration and evaluation of automated Monte Carlo simulations in the clinical practice of scanned proton and carbon ion beam therapy. *Phys Med Biol*, 59(16), 4635–4659.
- Bethe, H. A., Rose, E., & Smith, L. P. (1938). The Multiple Scattering of Electrons. *Proceedings of the American Philosophical Society*, 78(4), 573–585.
- Bragg, W., & Kleeman, R. (1905). On the alpha particles of radium, and their loss of range in passing through various atoms and molecules. *Philos Mag*, 5(6), 318–340.
- Brusasco, C. (1999). *A detector system for the verification of three-dimensional dose distributions in the tumor therapy with heavy ions*. Unpublished doctoral dissertation, Kassel University, Germany.
- Cavinato, M., Fabrici, E., Gadioli, E., Erba, E. G., & Risi, E. (1998). Boltzmann master equation theory of angular distributions in heavy-ion reactions. *Nuclear Physics A*, 643(1), 15–29.
- Cavinato, M., Fabrici, E., Gadioli, E., Erba, E. G., & Riva, G. (2001). Monte Carlo calculations of heavy ion cross-sections based on the Boltzmann Master equation theory. *Nuclear Physics A*, 679(3–4), 753–764.
- Cerutti, F., Battistoni, G., Capezzali, G., Colleoni, P., Ferrari, A., Gadioli, E., et al. (2006). Low Energy Nucleus-Nucleus Reactions: The BME Approach and its Interface with FLUKA. *Ric. Sci. Educ. Perm., Suppl.*, 126, 507–514.

References

- Devore, J., & Berk, K. (2011). *Modern Mathematical Statistics with Applications*. Springer.
- Education, T. H. (2013). *World University Rankings 2012-2013*. Retrieved December 2013, from <http://www.timeshighereducation.co.uk/world-university-rankings>
- Fassò, A., Ferrari, A., Ranft, J., & Sala, P. (1997). New developments in FLUKA modelling of hadronic and EM interactions. In *Proceedings of 3rd Workshop on Simulating Accelerator Radiation Environment*. Tsukuba, Japan.
- Fermi, E. (1950). High Energy Nuclear Events. *Progress of Theoretical Physics*, 5(4), 570–583.
- Ferrari, A., Ranft, J., Roesler, S., & Sala, P. (1996). Cascade particles, nuclear evaporation, and residual nuclei in high energy hadron-nucleus interactions. *Zeitschrift für Physik C Particles and Fields*, 70(3), 413–426.
- Ferrari, A., & Sala, P. (1997). The Physics of High Energy Reactions.
- Ferrari, A., Sala, P., Fasso, A., & Ranft, J. (2011). *FLUKA: a multi-particle transport code* (Tech. Rep.).
- Ferrari, A., Sala, P., Guaraldi, R., & Padoani, F. (1992). An improved multiple scattering model for charged particle transport. *Nuclear Instruments and Methods in Physics Research Section B: Beam Interactions with Materials and Atoms*, 71(4), 412–426.
- Fokas, E., Kraft, G., An, H., & Engenhardt-Cabillic, R. (2009). Ion beam radiobiology and cancer: time to update ourselves. *Biochim Biophys Acta*, 1796(2), 216–229.
- Gadioli, E., & Hodgson, P. (1992). *Pre-equilibrium Nuclear Reactions*. Clarendon Press.
- Goiten, M. (2008). *Radiation Oncology: A Physicist's-Eye View* (1st ed.). Springer.
- Golovkov, M. S., Aleksandrov, D. V., Chulkov, L. V., Kraus, G., & Schardt, D. (1997). Fragmentation of 270 a MeV carbon ions in water. (GSI-97-08).
- Griffin, J. J. (1967). Statistical Model of Intermediate Structure. *Physical Review Letters*, 19, 57–57.
- Haberer, T., Becher, W., Schardt, D., & Kraft, G. (1993). Magnetic scanning system for heavy ion therapy. *Nucl. Instrum. Methods Phys. Res. A*, 330(1–2), 296–305.
- Hansen, P. C., & Saxild-Hansen, M. (2012). AIR Tools — A MATLAB package of algebraic iterative reconstruction methods. *Journal of Computational and Applied Mathematics*, 236(8), 2167–2178.
- ICRU Report 49. (1993). *Stopping Powers and Ranges for Protons and Alpha Particles*. International Commission on Radiation Units and Measurements.

References

- Jäkel, O., & Reiss, P. (2007). The influence of metal artefacts on the range of ion beams. *Phys Med Biol*, 52(3), 635–644.
- Kleffner, C., Ondreka, D., & Weinrich, U. (2009). The Heidelberg Ion Therapy (HIT) accelerator coming into operation. *AIP Conference Proceedings*, 1099(1), 426–428.
- Knoll, G. F. (2000). *Radiation Detection and Measurement* (3rd ed.). John Wiley & Sons, Inc.
- Krämer, M., & Scholz, M. (2000). Treatment planning for heavy-ion radiotherapy: calculation and optimization of biologically effective dose. *Phys Med Biol*, 45(11), 3319–3330.
- Kurz, C., Mairani, A., & Parodi, K. (2012). First experimental-based characterization of oxygen ion beam depth dose distributions at the Heidelberg Ion-Beam Therapy Center. *Physics in medicine and biology*, 57(15), 5017.
- Lawrence, J. H., Tobias, C. A., Born, J. L., McCombs, R. K., Roberts, J. E., Anger, H. O., et al. (1958). Pituitary irradiation with high-energy proton beams: a preliminary report. *Cancer Res*, 18(2), 121–134.
- Leo, W. (1987). *Techniques for Nuclear and Particle Physics Experiments*. Springer Science & Business Media.
- Mairani, A., Brons, S., Cerutti, F., Fasso, A., Ferrari, A., Kramer, M., et al. (2010). The FLUKA Monte Carlo code coupled with the local effect model for biological calculations in carbon ion therapy. *Phys Med Biol*, 55(15), 4273–4289.
- Mairani, A., Parodi, K., Brons, S., Cerutti, F., Ferrari, A., Gadioli, E., et al. (2008). Clinical calculations of physical and biological effective dose distributions in proton and carbon ion therapy using the FLUKA Monte Carlo code. *Nuclear Science Symposium Conference Record, 2008. NSS '08. IEEE*, 5612–5615.
- Murray, R. M., Li, Z., & Sastry, S. S. (1994). *A Mathematical Introduction to Robotic Manipulation* (1st ed.). CRC Press.
- Ohno, Y., Kohno, T., Matsufuji, N., & Kanai, T. (2004). Measurement of electron density distribution using heavy ion CT. *Nucl. Instrum. Methods Phys. Res. A*, 525(1–2), 279–283.
- Parodi, K. (2004). *On the feasibility of dose quantification with in-beam PET data in radiotherapy with ^{12}C and proton beams*. Unpublished doctoral dissertation, Dresden University of Technology, Germany.
- Parodi, K. (2008). *Positron-Emission-Tomography for in-vivo verification of ion beam ther-*

References

- apy - Modeling, experimental studies and clinical implementation*. Unpublished doctoral dissertation, University of Heidelberg, Germany. (Habilitation thesis)
- Parodi, K. (2014). Heavy ion radiography and tomography. *Phys Med*, 30(5), 539–543.
- Parodi, K., Ferrari, A., Sommerer, F., & Paganetti, H. (2007). Clinical CT-based calculations of dose and positron emitter distributions in proton therapy using the FLUKA Monte Carlo code. *Phys Med Biol*, 52(12), 3369–3387.
- Parodi, K., Mairani, A., & Sommerer, F. (2013). Monte Carlo-based parametrization of the lateral dose spread for clinical treatment planning of scanned proton and carbon ion beams. *J Radiat Res*, 54 Suppl 1, i91–6.
- Paul, H., Geithner, O., & Jäkel, O. (2007). The influence of stopping powers upon dosimetry for radiation therapy with energetic ions. *Advances in Quantum Chemistry*, 52, 289–306.
- Rietzel, E., Schardt, D., & Haberer, T. (2007). Range accuracy in carbon ion treatment planning based on CT-calibration with real tissue samples. *Radiat Oncol*, 2, 14.
- Rinaldi, I. (2011). *Investigation of novel imaging methods using therapeutic ion beams*. Unpublished doctoral dissertation, University of Heidelberg, Germany.
- Rinaldi, I., Brons, S., Gordon, J., Panse, R., Voss, B., Jakel, O., et al. (2013). Experimental characterization of a prototype detector system for carbon ion radiography and tomography. *Phys Med Biol*, 58(3), 413–427.
- Rinaldi, I., Brons, S., Jakel, O., Voss, B., & Parodi, K. (2014). Experimental investigations on carbon ion scanning radiography using a range telescope. *Phys Med Biol*, 59(12), 3041–3057.
- Rinaldi, I., Ferrari, A., Mairani, A., Paganetti, H., Parodi, K., & Sala, P. (2011). An integral test of FLUKA nuclear models with 160 MeV proton beams in multi-layer Faraday cups. *Phys Med Biol*, 56(13), 4001–4011.
- Roelofs, E., Engelsman, M., Rasch, C., Persoon, L., Qamhiyeh, S., Ruysscher, D. de, et al. (2012). Results of a Multicentric In Silico Clinical Trial (ROCOCO): Comparing Radiotherapy with Photons and Protons for Non-small Cell Lung Cancer. *Journal of Thoracic Oncology*, 7(1), 165–176.
- Schardt, D., Steidel, P., Krämer, M., Weber, U., Parodi, K., & Brons, S. (2007). *Precision Bragg-curve measurements for light-ions in water* (Tech. Rep.). GSI report 2008.
- Schneider, U., Besserer, J., Pemler, P., Dellert, M., Moosburger, M., Pedroni, E., et al.

References

- (2004). First proton radiography of an animal patient. *Med Phys*, *31*(5), 1046–1051.
- Schneider, U., & Pedroni, E. (1995). Proton radiography as a tool for quality control in proton therapy. *Med Phys*, *22*(4), 353–363.
- Schulte, R., Bashkirov, V., Li, T., Liang, Z., Mueller, K., Heimann, J., et al. (2004). Conceptual design of a proton computed tomography system for applications in proton radiation therapy. *Nuclear Science, IEEE Transactions on*, *51*(3), 866–872.
- Schwaab, J., Brons, S., Fieres, J., & Parodi, K. (2011). Experimental characterization of lateral profiles of scanned proton and carbon ion pencil beams for improved beam models in ion therapy treatment planning. *Phys Med Biol*, *56*(24), 7813–7827.
- Seeley, R., Stephens, T., & Tate, P. (2007). *Anatomy and Physiology*. McGraw-Hill.
- Shinoda, H., Kanai, T., & Kohno, T. (2006). Application of heavy-ion CT. *Phys Med Biol*, *51*(16), 4073–4081.
- Sommerer, F., Parodi, K., Ferrari, A., Poljanc, K., Enghardt, W., & Aiginger, H. (2006). Investigating the accuracy of the FLUKA code for transport of therapeutic ion beams in matter. *Phys Med Biol*, *51*(17), 4385–4398.
- Testa, M., Verburg, J. M., Rose, M., Min, C. H., Tang, S., Bentefour, E. H., et al. (2013). Proton radiography and proton computed tomography based on time-resolved dose measurements. *Phys Med Biol*, *58*(22), 8215–8233.
- Turner, J. E. (2007). *Atoms, Radiation, and Radiation Protection* (3rd ed.). Wiley-VCH Verlag GmbH & Co, KGaA.
- Weisskopf, V. F., & Ewing, D. H. (1940). Erratum: On the Yield of Nuclear Reactions with Heavy Elements (Phys. Rev. *57*, 472 (1940)). *Phys. Rev.*, *57*, 935–935.
- WHO. (2008). *World Cancer Report 2008*. International Agency for Research of Cancer.
- Wilson, R. R. (1946). Radiological use of fast protons. *Radiology*, *47*(5), 487–491.
- Ziegler, J. (2004). SRIM-2003. *Nucl. Instrum. Methods Phys. Res. B*, *219*, 1027–1036.

Appendices

Appendix A

FLUKA *source.f* user routine

The user routine *source.f* is used to sample primary particle properties from distributions too complicated to be described by the standard FLUKA input cards.

This FORTRAN code samples the primary particle properties from a phase space file and reproduces the scanning system from HIT by rotating every sampled particle to the correct beam direction, according to RP coordinates.

Listing A.1: Relevant code from the user routine *source.f*

```
1      SUBROUTINE SOURCE ( NOMORE )
2
3      * Declaration of different variables
4      INTEGER TOTAL_PARTICLES, TOTAL_POINTS
5      LOGICAL LFIRST
6      DOUBLE PRECISION ENE(20000000), XPOS(20000000),YPOS(20000000)
7      DOUBLE PRECISION XCOS(20000000),YCOS(20000000)
8      DOUBLE PRECISION RAND1, RAND2, RAND3
9      DOUBLE PRECISION POINT_XY(2)
10     DOUBLE PRECISION INDEX_X, INDEX_Y
11     DOUBLE PRECISION ABV(3), ABV_N(3), TOROT(3)
12     DOUBLE PRECISION ARB_AXIS(3), AXIS_N(3), NORMALI, NORMALI2
13     DOUBLE PRECISION OLDBEAM(3), VROT(3), DOT_PRO
14     DOUBLE PRECISION SCR_VEC(60)
15     DOUBLE PRECISION DEP_DOSE
16
17     * SCR_VEC and DEP_DOSE are common arrays
18     * These arrays are shared between source.f and comscw.f
19     COMMON /TIAGO/ SCR_VEC
20     COMMON /TIAGO/ DEP_DOSE
```

APPENDIX A. FLUKA *SOURCE.F* USER ROUTINE

```

21
22 * Open binary file to write output
23     OPEN ( UNIT = IODRAW, FILE = 'SCORE.bin',
24           &     STATUS = 'UNKNOWN', FORM = 'UNFORMATTED' )
25
26 *     Binary format of data file header
27 *         1   int32 = begin of header
28 *         1 float64 = WHASOU(1): field size in X direction (cm)
29 *         1 float64 = WHASOU(2): field size in Y direction (cm)
30 *         1 float64 = WHASOU(3): step in X direction (cm)
31 *         1 float64 = WHASOU(4): step in Y direction (cm)
32 *         1 float64 = WHASOU(5): number of primaries per raster point
33 *         1 float64 = WHASOU(6): Z position of the detector (cm)
34 *         1 float64 = WHASOU(7): Detector number (0 or 1)
35 *         1   int32 = end of header
36
37 *     Binary format of 1 RP energy scoring (repeat for each RP)
38 *         1   int32 = begin of RP scoring
39 *         1 float64 = Index X
40 *         1 float64 = Index Y
41 *         1 float64 = Dose deposited inside phantom (Gy)
42 *         60 float64 = Energy scoring for each detector channel
43 *         1   int32 = end of RP scoring
44
45 *-----*
46
47 * First call initializations:
48     IF ( LFIRST ) THEN
49
50 * Write binary file header in the first iteration
51     WRITE(IODRAW) WHASOU(1), WHASOU(2), WHASOU(3), WHASOU(4),
52           &     WHASOU(5), WHASOU(6), WHASOU(7)
53
54 * Starting indexes for scanning pattern
55     INDEX_X = 1
56     INDEX_Y = 1
57
58 * Total points and total particles
59     TOTAL_POINTS = INT((WHASOU(1)/WHASOU(3)+1)*(WHASOU(2)/WHASOU(4)
60           &     +1))
61     TOTAL_PARTICLES = INT(TOTAL_POINTS*WHASOU(5))
62
63 * Initialization of different variables
64     SCR_VEC = ZERZER
65     DEP_DOSE = ZERZER

```

APPENDIX A. FLUKA *SOURCE.F* USER ROUTINE

```

66         ICOUNTER = ZERZER
67
68 * Read all values from phase space file and store them in arrays
69 300      CONTINUE
70         READ(39, END=400) ENE(ICOUNTER+1),XPOS(ICOUNTER+1),
71         &          YPOS(ICOUNTER+1),XCOS(ICOUNTER+1),YCOS(ICOUNTER+1)
72
73         ICOUNTER=ICOUNTER+1
74
75         GO TO 300
76
77     END IF
78 *-----*
79
80 * Random sample
81     ISAMPLE = AINT(FLRNDM(DUMMY)*ICOUNTER)+1
82
83 * Scanning pattern
84     IF (MOD(INDEX_Y,TWOTWO) .GT. 1E-09) THEN
85         POINT_XY(1) = -WHASOU(1)/TWOTWO+(INDEX_X-1)*WHASOU(3)
86     ELSE
87         POINT_XY(1) =  WHASOU(1)/TWOTWO-(INDEX_X-1)*WHASOU(3)
88     END IF
89
90     POINT_XY(2) =  WHASOU(2)/TWOTWO-(INDEX_Y-1)*WHASOU(4)
91
92 *-----*
93
94 * Rotation of the sampled direction cosine from the phase space
95
96 * Vector AB that joins A=(0,0,-650.6) with B=(Xpos,Ypos,0)
97     ABV(1) = POINT_XY(1)
98     ABV(2) = POINT_XY(2)
99     ABV(3) = 650.6
100
101 * Normalization of vector AB
102     NORMALI = SQRT(ABV(1)**2+ABV(2)**2+ABV(3)**2)
103
104     ABV_N(1) = ABV(1)/NORMALI
105     ABV_N(2) = ABV(2)/NORMALI
106     ABV_N(3) = ABV(3)/NORMALI
107
108 * Vector sampled from phase space - vector that will be rotated
109     TOROT(1) = XCOS(ISAMPLE)
110     TOROT(2) = YCOS(ISAMPLE)

```

APPENDIX A. FLUKA *SOURCE.F* USER ROUTINE

```

111      TOROT(3) = SQRT(ONEONE - XCOS(ISAMPLE)**2 - YCOS(ISAMPLE)**2)
112
113      * Forward direction vector (FORWARD)
114      OLDBEAM(1) = ZERZER
115      OLDBEAM(2) = ZERZER
116      OLDBEAM(3) = ONEONE
117
118      * Cross product (AB x FORWARD) gives the arbitrary axis for rotation
119      ARB_AXIS(1) = ABV_N(2)*OLDBEAM(3) - ABV_N(3)*OLDBEAM(2)
120      ARB_AXIS(2) = ABV_N(3)*OLDBEAM(1) - ABV_N(1)*OLDBEAM(3)
121      ARB_AXIS(3) = ABV_N(1)*OLDBEAM(2) - ABV_N(2)*OLDBEAM(1)
122
123      * Normalization of the axis rotation vector
124      NORMALI2 = SQRT(ARB_AXIS(1)**2+ARB_AXIS(2)**2+ARB_AXIS(3)**2)
125
126      * IF avoids float point exception in the normalization (division by 0)
127      IF (NORMALI2 .LT. 1E-9) THEN
128          AXIS_N(1) = 0
129          AXIS_N(2) = 0
130          AXIS_N(3) = 1
131      ELSE
132          AXIS_N(1) = ARB_AXIS(1)/NORMALI2
133          AXIS_N(2) = ARB_AXIS(2)/NORMALI2
134          AXIS_N(3) = ARB_AXIS(3)/NORMALI2
135      END IF
136
137      * Dot product gives the angle between AB and FORWARD = Rotation angle
138      ROT_AG = -ACOS((ABV(1)*OLDBEAM(1)+ABV(2)*OLDBEAM(2)+
139      &          ABV(3)*OLDBEAM(3))/(SQRT(ABV(1)**2+ABV(2)**2+ABV(3)**2)*
140      &          SQRT(OLDBEAM(1)**2+OLDBEAM(2)**2+OLDBEAM(3)**2)))
141
142      * Rodrigues' rotation formula
143      DOT_PRO = TOROT(1)*AXIS_N(1)+TOROT(2)*AXIS_N(2)+TOROT(3)*AXIS_N(3)
144
145      VROT(1) = TOROT(1)*COS(ROT_AG)+SIN(ROT_AG)*(AXIS_N(2)*TOROT(3)-
146      &          AXIS_N(3)*TOROT(2))+AXIS_N(1)*DOT_PRO*(1-COS(ROT_AG))
147      VROT(2) = TOROT(2)*COS(ROT_AG)+SIN(ROT_AG)*(AXIS_N(3)*TOROT(1)-
148      &          AXIS_N(1)*TOROT(3))+AXIS_N(2)*DOT_PRO*(1-COS(ROT_AG))
149      VROT(3) = TOROT(3)*COS(ROT_AG)+SIN(ROT_AG)*(AXIS_N(1)*TOROT(2)-
150      &          AXIS_N(2)*TOROT(1))+AXIS_N(3)*DOT_PRO*(1-COS(ROT_AG))
151
152      *-----*
153
154      * Cosine director sample for the scanning beam
155      TXFLK (NPFLKA) = VROT(1)

```

APPENDIX A. FLUKA *SOURCE.F* USER ROUTINE

```

156      TYFLK (NPFLKA) = VROT(2)
157      TZFLK (NPFLKA) = VROT(3)
158
159      * Particle coordinate from which transport was started
160      XFLK(NPFLKA) = XPOS(ISAMPLE)-112.6/650.6*POINT_XY(1)+POINT_XY(1)
161      YFLK(NPFLKA) = YPOS(ISAMPLE)-112.6/650.6*POINT_XY(2)+POINT_XY(2)
162      ZFLK(NPFLKA) = -112.6
163
164      *-----*
165
166      * Update indexes, write data to binary file and end the simulation
167      IF (MOD(NCASE, INT(WHASOU(5))) .LT. 1) THEN
168          WRITE(IODRAW) INDEX_X, INDEX_Y, DEP_DOSE, SCR_VEC
169          INDEX_X = INDEX_X + 1
170          SCR_VEC = ZERZER
171          DEP_DOSE = ZERZER
172      END IF
173
174      * Update scanning index in X and Y direction
175      IF (INDEX_X .GT. WHASOU(1)/WHASOU(3)+1) THEN
176          INDEX_X = 1
177          INDEX_Y = INDEX_Y + 1
178      END IF
179
180      * End of simulation. Total number of primaries reached
181      IF (NCASE .EQ. TOTAL_PARTICLES + 1) THEN
182          NOMORE = 1
183      END IF
184
185      *-----*
186
187      RETURN
188      *=== End of subroutine Source =====*
189      END

```


Appendix B

FLUKA *comscw.f* user routine

With the user routine *comscw.f* it is possible to implement any desired logic to differentiate the returned scoring value.

This FORTRAN code checks if FLUKA is scoring energy deposition and where. If the scoring belongs to a channel from the detector, the value is saved. Every time we move from one RP to another, the *source.f* routine writes the values from the energy deposited in the detector for that RP. This way, we obtain a BC for every RP. The code can also score the dose deposited in the phantom for a full radiography.

Listing B.1: Relevant code from the user routine *comscw.f*

```
1      DOUBLE PRECISION FUNCTION COMSCW(IJ,XA,YA,ZA,MREG,RULL,LLO,ICALL)
2
3      * Declaration of different variables
4      INTEGER CH_INDEX
5      DOUBLE PRECISION DET_TYPE
6      DOUBLE PRECISION DET_CHSZ
7      DOUBLE PRECISION SCR_VEC(60)
8      DOUBLE PRECISION DEP_DOSE
9
10     * SCR_VEC and DEP_DOSE are common arrays
11     * These arrays are shared between source.f and comscw.f
12     COMMON /TIAGO/ SCR_VEC
13     COMMON /TIAGO/ DEP_DOSE
14
15     * Check for IC stack size
16     IF (WHASOU(7) .LT. 0.5) THEN
17         DET_CHSZ = 0.1
```

APPENDIX B. FLUKA *COMSCW.F* USER ROUTINE

```

18      DET_TYPE = DET_CHSZ*60
19      ELSE
20      DET_CHSZ = 0.3
21      DET_TYPE = DET_CHSZ*60
22      END IF
23
24      * Score only energy and checks for correct bin number
25      * DETECTOR must be the FIRST USRBIN card in the input file
26      IF ( ISCRNG .EQ. 1 .AND. JSCRNG .EQ. 1) THEN
27
28      * Check if energy is being deposited inside the scoring box (IC stack):
29      *      X = -15 to 15 cm
30      *      Y = -15 to 15 cm
31      *      Z = whasou(6) to whasou(6) + DET_TYPE cm
32      IF(Xa .GT. -15 .AND. Xa .LT. 15 . AND. Ya .GT. -15 .AND.
33      &                                     Ya .LT. 15 .AND. Za .GT. WHASOU(6) .AND.
34      &                                     Za .LT. WHASOU(6)+DET_TYPE) THEN
35
36      * Detector channel ranging from 1 to 60 (0.1 cm thickness) or 1 to 60
37      * (0.3 cm thickness) according to WHASOU(7)
38      CH_INDEX = INT(FLOOR((Za-WHASOU(6))/DET_CHSZ+1))
39
40      * Score energy to correct detector channel
41      * source routine writes this vector to the binary file
42      * every time we move to another RP
43      SCR_VEC(CH_INDEX) = SCR_VEC(CH_INDEX) + RULL
44
45      END IF
46
47      END IF
48
49      * Score dose deposited inside phantom
50      * PHANTOM must be the SECOND USRBIN card in the input file
51      IF (ISCRNG .EQ. 1 .AND. JSCRNG .EQ. 2) THEN
52
53      * PHANTOM must be REGION 5 in the geometry
54      IF (MREG .EQ. 5) THEN
55      DEP_DOSE = DEP_DOSE+RULL*ELCMKS*1.D12/RHO(MEDFLK(MREG,1))
56      END IF
57
58      END IF
59
60      RETURN
61      *==== End of function Comscw =====*
62      END

```


Appendix C

Submitting a job to the Compute cluster

To be able to submit a FLUKA simulation to the compute cluster we have to create a bash script to copy the input files to the cluster home and to run FLUKA on that location. Below, we can see a script that runs 180 FLUKA jobs in the cluster.

Listing C.1: Bash script to submit a job to the cluster

```
1  #!/bin/bash
2  source /etc/profile.d/modules.sh
3
4  # Load queuing system SLURM
5  module load slurm
6
7  # Input directory path and input file name
8  INPUTDIR=/home/t/Tiago.Marcelos/Projects/Cluster_Sim/Radiography
9  FILENAME=beam
10
11 # Number of different jobs
12 t=1
13 while [ $t -ne 0 ]
14 do
15     INPUTNUM=180
16     LOOPNUM='expr $INPUTNUM + 1'
17     t=$?
18 done
19
20 # Create and define the directory to run the jobs in the cluster home
21 DATESTRING=$(date +%Y%m%d_%H:%M:%S)
22 mkdir /project/med-clhome/t/Tiago.Marcelos/Radiography/$DATESTRING
23 RUNDIR=/project/med-clhome/t/Tiago.Marcelos/Radiography/$DATESTRING
```

APPENDIX C. SUBMITTING A JOB TO THE COMPUTE CLUSTER

```
24
25 # Define CODE
26 export FLUPRO=/software/opt/precise/x86_64/fluka/2011.2b.5
27 CODE=${FLUPRO}/flutil/rfluka
28
29 # Run python script to change the initial seed for every job
30 python seed_changing.py $FILENAME.inp $INPUTNUM
31
32 # Copy input files to RUNDIR
33 i=1
34 while [ $i -ne $LOOPNUM ]
35 do
36     cp $FILENAME'_'$i.inp $RUNDIR
37     i='expr $i + 1'
38 done
39
40 # Copy FLUKA executable to RUNDIR
41 cp RadiographyEXEC $RUNDIR
42
43 # Submit the jobs to the cluster
44 i=1
45 while [ $i -ne $LOOPNUM ]
46 do
47     cat <<EOL|sbatch
48     #!/bin/bash
49     #SBATCH --job-name='$FILENAME'_'$i'
50     #SBATCH --workdir=/project/med-clhome/t/Tiago.Marcelos/
51     #SBATCH --export=NONE
52     #SBATCH --mail-type=FAIL
53
54     # load module system and fluka
55     source /etc/profile.d/modules.sh
56     module load fluka/2011.2b.5
57
58     # Running Fluka
59     cd $RUNDIR
60     $CODE -e $RUNDIR/RadiographyEXEC -M 1 $RUNDIR/$FILENAME'_'$i.inp
61     wait
62
63     EOL
64
65     wait
66     i='expr $i + 1'
67 done
```

Appendix D

Read binary output files from FLUKA

This MATLAB script allows us to read the binary output data from FLUKA, organize it, find the channel number of the BP position for each RP and then convert this number to WET. The final result is a radiography where each pixel corresponds to a RP. The code is similar for a CT simulation but, in the end, instead of a radiography we obtain a sinogram. Finally, the data is saved and can be post processed and plotted.

Listing D.1: MATLAB script to read binary output files from FLUKA

```
1  clc
2  close all
3  clear all
4
5  % Path location and extension of the binary files
6  PATH = '~/Projects/Radiography/Final_Rad_Reconstruction/Files/Step_2mm/';
7  EXT = '*SCORE.bin';
8
9  addpath(PATH);
10
11 % List files in directory
12 matfiles = dir(sprintf('%s%s',PATH,EXT));
13
14 % Iterate over each binary file
15 for j=1:length(matfiles)
16
17     % Open binary file and check for opening error
18     fid = fopen(matfiles(j).name, 'r');
19
20     if (fid == -1)
```

APPENDIX D. READ BINARY OUTPUT FILES FROM FLUKA

```

21     disp('Error opening file');
22     return
23 end
24
25 %Read binary file header
26 fread(fid, 1, 'int32');           % begin of header
27 xdim = fread(fid, 1, 'float64');   % field size in X direction (cm)
28 ydim = fread(fid, 1, 'float64');   % field size in Y direction (cm)
29 xstep = fread(fid, 1, 'float64');  % step size in X direction (cm)
30 ystep = fread(fid, 1, 'float64');  % step size in Y direction (cm)
31 Npart = fread(fid, 1, 'float64');  % number of primaries per RP
32 ZdetPOS = fread(fid,1,'float64');  % Z position of the detector (cm)
33 DET_type = fread(fid,1,'float64'); % Detector number (0 or 1)
34 fread(fid, 1, 'int32');           % end of header
35
36 % Calculate number of RPs in X and Y
37 Xpoints = floor(xdim/xstep+1);
38 Ypoints = floor(ydim/ystep+1);
39
40 % Calculate the total number of RPs
41 RPpoints = Xpoints*Ypoints;
42
43 % Initializes variables
44 CH=zeros(Xpoints,Ypoints, 60);
45
46 if j==1
47     CHdist=zeros(Xpoints,Ypoints, 60);
48     DepDose=0;
49 end
50
51 % Read data from the binary file for each RP
52 for i=1:RPpoints
53     fread(fid, 1, 'int32');           % Begin of RP scoring
54     Xindex=fread(fid, 1, 'float64');   % Index X
55     Yindex=fread(fid, 1, 'float64');   % Index Y
56     Dose=fread(fid, 1, 'float64');     % Dose dep. in phantom (Gy)
57     CH(Xindex,Yindex,:)=fread(fid, 60, 'float64'); % Energy scoring
58                                     %for each detector channel
59     fread(fid, 1, 'int32');           % End of RP scoring
60
61     % Increment dose
62     DepDose=DepDose+Dose;
63 end
64
65 % Add CH information to CHdist matrix

```

APPENDIX D. READ BINARY OUTPUT FILES FROM FLUKA

```

66     CHdist=CHdist+CH;
67
68     fclose(fid);
69
70 end
71
72 % Initializes variable MAXmapN (Map with the BP positions)
73 MAXmapN=zeros(Xpoints,Ypoints);
74
75 % Find the BP position (Channel number) for each (X,Y) coordinate
76 for k=1:Ypoints
77     for l=1:Xpoints
78         B = CHdist(l,k,:);
79         [~,MAXmapN(l,k)]=max(B(:));
80     end
81 end
82
83 MAXmapN=MAXmapN';
84
85 %Flip even rows left to right (due to scanning pattern)
86 k=2;
87 while (1)
88     MAXmapN(k,:) = fliplr(MAXmapN(k,:));
89     k=k+2;
90     if k > Ypoints
91         break
92     end
93 end
94
95 % Converts the BP channel number to WET in mm
96 a = 0.002177; % (MeV/u)-1.75
97 b = 0.9174;
98 Ene = 334.94; % MeV/u
99
100 RadiographyWET = 1.165*3*(a*Ene1.75+b-MAXmapN); % eq. 3.12
101
102 save('Radiography.mat','RadiographyWET')

```